Research article

Phase stability of the Al$_x$CrFeCoNi alloy system

M.E. Bloomfield[a], K.A. Christofidou[b], P.M. Mignanelli[c], A-P.M. Reponen[a], H.J. Stone[a], N.G. Jones[a,*]

[a] *Department of Materials Science and Metallurgy, University of Cambridge, 27 Charles Babbage Road, Cambridge CB3 0FS, UK*
[b] *Department of Materials Science and Engineering, The University of Sheffield, Sir Robert Hadfield Building, Mappin Street, S1 3JD, UK*
[c] *Rolls-Royce plc, Derby DE24 8BJ, UK*

ABSTRACT

The addition of Al to the A1 CrFeCoNi alloy has been shown to promote the formation of intermetallic phases, offering possibilities for the development of alloys with advantageous mechanical properties. However, despite numerous experimental investigations, there remain significant uncertainties as to the phase equilibria in this system particularly at temperatures below 1000°C. The present study makes a systematic assessment of the literature data pertaining to the equilibrium phases in alloys of the Al$_x$CrFeCoNi system. Two alloys, with atomic ratios, $x = 0.5$ and 1.0, are then selected for further experimental investigation, following homogenisation (1200°C/72 h) and subsequent long-duration (1000 h) heat-treatments at 1000, 850 and 700°C. The Al$_{0.5}$ alloy was found to be dual-phase A1 + B2 in the homogenised condition and following exposure at 1000°C but D8$_b$ phase precipitates developed following heat-treatment at the lower temperatures. In the Al$_{1.0}$ alloy, B2, A2 and A1 phases were identified in the homogenised condition and at 1000°C. At 850 and 750°C, the A2 phase was replaced by the D8$_b$ phase. These experimental observations were used alongside literature data to assess the veracity of CALPHAD predictions made using the TCHEA4 thermodynamic database.

1. Introduction

The Al$_x$CrFeCoNi alloys are among the most widely studied within the High-Entropy Alloy (HEA) literature. Their duplex *fcc* (A1) + B2 microstructures, and the possibility of introducing other phases such as L1$_2$, *bcc* (A2) and σ (D8$_b$), are highly advantageous for developing alloys with balanced properties. It is well known that increasing the proportion of Al promotes the formation of the B2 and A2 phases and enhances the strength of the alloy, albeit at the expense of ductility [1–3]. The alloy system is also well suited to solid solution strengthening and coherent precipitation reinforcement, making it a potential candidate for elevated-temperature structural applications in the nuclear, turbine and aerospace industries [4–6]. In terms of the relationship between composition and phase constitution, Al and, in particular, the Al:Cr ratio, have the greatest influence upon phase stability [7]. As such, many studies have focused on tuning mechanical properties through the control of microstructure by adjusting the Al-content [2,8–14] and processing conditions [15–21]. This has led to some promising results. In particular, it has been shown that the Al$_{1.0}$ alloy can achieve a superior specific

strength compared to commercial alloys at intermediate temperatures [22]. Furthermore, the Al$_{0.3}$ alloy has strong potential for protection applications such as armours through its remarkable resistance to shear failure [23]. However, the pursuit of enhanced mechanical properties has often led to the formation of highly complex microstructures, which may be far from equilibrium. For example, many studies have focused on the as-cast condition [3,8,24–29], which frequently contains solidification-induced elemental segregation. This can alter the subsequent microstructural evolution and lead to spatial variations if an appropriate homogenisation heat-treatment is not applied prior to annealing. In fact, it has recently been demonstrated that the initial condition of Al$_{0.3}$ alloy specimens can substantially alter the phase precipitation pathway during heat-treatment, depending on whether or not recrystallisation is carried out prior to annealing [20]. Furthermore, it has been shown that timescales of hundreds of hours can be required for the formation of equilibrium phases [12,30,31]. Therefore, despite numerous investigations, there remains much uncertainty as to the equilibrium phase constitution of the Al$_x$CrFeCoNi alloys.

A clearer picture of phase stability in this system is essential to streamlining future alloy design and optimisation activities. Therefore, in this study a critical review of the existing literature relating to the phase stability of the Al$_x$CrFeCoNi system is presented

Table 1
Nomenclature of phases observed in alloys of the $Al_xCrFeCoNi$ system.

Common name	Prototype	Strukturbericht Designation	Thermo-Calc name
fcc	Cu	A1	FCC_A1
bcc	W	A2	BCC_A2
B2	ClCs	B2	BCC_B2
σ	CrFe	$D8_b$	SIGMA
$L1_2$	$AuCu_3$	$L1_2$	FCC_L12

and several, carefully chosen long-duration heat-treatments are performed to better establish the thermodynamic stability at certain temperatures and compositions. Together with information obtained from the literature, these experimental results are used to assess the veracity of phase stability predictions of the TCHEA4 thermodynamic database.

1.1. Nomenclature

Several nomenclatures for crystallographic phases are in common usage in the literature. In some cases, this appears to have led to confusion as to the nature and identity of certain phases (see section 1.3). Therefore, for clarification, frequently used names for phases of the $Al_xCrFeCoNi$ system are provided in Table 1. In this publication, all phases are referred to by their Strukturbericht Designation.

1.2. Current knowledge of phase stability of the $Al_xCrFeCoNi$ system

The $Al_xCrFeCoNi$ alloys are based upon the equiatomic CrFeCoNi alloy, which has been shown to be thermodynamically stable as a single A1 phase in the temperature range 500 – 1100°C [32–34]. Several studies have investigated the effect of Al on the microstructural equilibrium, by systematically varying the Al-content while maintaining the other elements in an equiatomic ratio [2,10–14,35,36]. These studies have shown that the solid solution matrix phase transitions from A1 at low Al concentrations to B2 at higher Al concentrations, via a dual phase A1 + B2 microstructure. Whilst the phase-transition temperatures are likely to vary with annealing temperature as well as composition, existing literature data suggests that the $Al_xCrFeCoNi$ system is single phase A1 for $0 \geq x \geq 0.2$ (all concentrations in atomic ratios unless otherwise stated). Evidence of B2 precipitates is first seen at $x = 0.25$ [11] (whilst the phase is not reported by the authors in this condition, a B2 superlattice peak is visible at ~ 52° in the XRD data presented in Fig. 5 of reference [11]), and its volume fraction increases with increasing Al concentration [12], becoming the majority phase at $x \approx 0.7$. Certain precipitate phases have also been reported in the literature. The $L1_2$ phase has been observed below 700°C for $0.12 \geq x \geq 0.7$ [20,21,35,37–39]. Intermetallic $D8_b$ phase precipitates have also been observed at 700°C and below in $Al_{0.3}$ [19,20,40,41] and $Al_{0.45}$ [36] alloys, at 850°C in $Al_{0.6}$ [42], 700°C in $Al_{0.73}$ [36], $\leq$ 700°C in $Al_{0.875}$ [10], 900°C in $Al_{0.9}$ [9], and following exposure at temperatures as high as 1150°C in the $Al_{1.0}$ alloy [12,22,36,43–47]. In alloys with $x \geq 1.0$, A2 precipitates are also commonly reported to form within the B2 matrix [9,19,36,48]. Attempts have also been made to compare the experimentally observed phase stability of Al_x alloys with thermodynamic CALPHAD predictions [30,36,47,49,50]. For example, Zhang *et al.* [30] developed a thermodynamic database that accurately predicted the phase stability of the $Al_{0.3}$ and $Al_{0.7}$ alloys and Butler & Weaver [36] employed long-duration heat-treatments to test the predictions of the TCNI8 database for alloys containing between 10 and 30 at.% Al.

In the present work, two $Al_xCrFeCoNi$ alloys with Al atomic ratios $x = 0.5$ and 1.0 (equivalent to Al concentrations of 11.1 and 20.0 at.%, respectively) were produced for further study. These alloys were

selected as their microstructures are among the most complex and promising for achieving well-balanced mechanical properties. The $Al_{0.5}$ alloy is dual phase A1 + B2, whereas the $Al_{1.0}$ alloy develops an A2 + B2 microstructure on solidification. Furthermore, as shall be elucidated in the following sections, there remains much uncertainty as to the equilibrium phase constitution of these alloys, particularly at intermediate temperatures.

1.3. $Al_{0.5}CrFeCoNi$

In the as-cast state, the $Al_{0.5}$ alloy has a dendritic microstructure that is generally reported to be comprised of Al-depleted A1 dendrites (DR) and AlNi-rich interdendritic regions (ID) [2,8,12,16,51,52]. Some studies report that the ID adopt the disordered A2 structure [16,52,53], whilst others suggest that they have an ordered B2 structure [2,54]. A fine-scale decomposition of the ID into AlNi and CrFe-rich phases has also been observed in some cases [8,25].

Confusion as to whether the ID phase takes the A2 or B2 structure often stems from an over-reliance on laboratory X-ray diffraction (XRD) for phase identification, as weak superlattice reflections can make it hard to distinguish the B2 from the A2 phase. In addition, there appears to be some inconsistency in how the A2 and B2 phases are classified within the literature. Several studies have used the term '*bcc*' to describe both phases. However, whilst the ordered B2 and disordered A2 phase are structurally related, referring to the B2 phase as '*bcc*' is incorrect because it has a primitive cubic crystal structure. Some of this confusion may stem from the phase names used in the Thermo-Calc thermodynamic databases (Table 1). The B2 phase observed in the present alloy system is based upon an Al and a Ni sublattice, which makes it easy to distinguish from the A2 phase that is typically enriched in Cr and Fe [9,12,13,30,47,48,55]. It should be noted, however, that the B2 phase in the AlCrFeCoNi system has substantial solubility for other elements, most notably Co [9,30,47,48,56]. The incorporation of these additional elements into the B2 structure necessarily reduces the degree of ordering on at least one sublattice. This partial ordering of the B2 phase has been investigated by King *et al.* [57], who used density functional theory (DFT) to study the stability of the A2 structure with varying Al-contents. Their results indicated that, for Al contents up to an atomic ratio of 2.0, the partitioning of Al and Ni to separate sublattices (to the B2 phase) was favored over a completely disordered A2 lattice. It was also demonstrated that decomposition of the phase into AlNi and CrFe-rich regions could be thermodynamically favourable at lower temperatures in Al-rich alloys. Ogura *et al.* [58] have also performed DFT calculations which indicate that a partially disordered B2 structure, where the Al atoms occupy one sublattice and the transition metal atoms are randomly distributed on the other, is more stable than the truly disordered A2 phase. With this in mind, it is interesting to consider what effect partial ordering can have on the mechanical properties and phase stability of the B2 phase.

Heat-treatment of as-cast material between 1100 and 1000°C [2,9,11,12,36,52] has resulted in microstructures containing A1 and B2 phases. Sintering of elemental powders at 1000°C has also been found to produce a A1 + B2 microstructure [12]. Lin *et al.* [16] studied the $Al_{0.5}$ alloy following 24 h heat-treatments of the as-cast material between 350 and 950°C. At each temperature, fine Al-rich 'needle-shaped' precipitates formed throughout the DR and 'wall-shaped' precipitates formed within the AlNi-rich ID. XRD reflections corresponding to an A1 structure were observed in the as-cast state and following each heat-treatment additional reflections appeared, which were consistent with an A2 structure (with no evidence of superlattice reflections). Based on this evidence, the authors concluded that the DR and ID were A1, whereas the 'needle' and 'wall-shaped' precipitates were both identified as being A2. However, the elemental concentration quantifications showed a marked difference in the partitioning of the DR and ID. The DR was depleted of Al,

whereas the ID were highly enriched in Al & Ni. Moreover, the partitioning of the needle and wall-shaped precipitates closely resembled the partitioning of the ID and DR, respectively. This indicated that the DR and 'wall-shaped' precipitates were, in fact, A1. The AlNi-rich composition of the ID and 'needle-shaped' precipitates, on the other hand, suggested that they both adopted the B2 structure. As discussed previously, the B2 superlattice reflections are much weaker than the fundamental reflections, so are not always visible in laboratory diffraction data. A subsequent investigation of $Al_{0.5}$ alloy specimens following 2 h heat-treatments at 1100 and 900°C used transition electron microscopy (TEM) selected-area diffraction patterns (SADPs) to conclusively identify the phases present [9]. At both exposure temperatures, the microstructures appeared similar to those observed in the previous study but the electron diffraction patterns from the 900°C specimen confirmed that the DR were A1 and the AlNi-rich ID and needle-like precipitates had the B2 structure. This finding was supported by a later study, which also found clear evidence of the B2 phase from XRD and TEM-SADPs following an 8 h heat-treatment at 850°C [53].

The literature discussed thus far has only shown evidence of the A1 and B2 phase, following thermal exposures of the $Al_{0.5}$ alloy between 350 and 1100°C. This is somewhat surprising, as the $D8_b$ phase has been widely observed both in the $Al_{0.3}$ alloy in the temperature range 550–700°C [19,20,40,59,60] and in the $Al_{1.0}$ alloy between 600 and 1150°C [22,36,43–45,47]. The $D8_b$ phase has also been observed in a $Al_{0.9}$ alloy following thermal exposure at 900°C for 2 h [9]; in a $Al_{0.875}$ alloy following homogenisation (1100°C / 24 h) and subsequent exposure at 600, 650 and 700°C for 1 h [10]; in a $Al_{0.6}$ alloy, following heat-treatment of as-cast material at 850°C for 4 h [42]; and in $Al_{0.73}$ and $Al_{0.45}$ alloys, following a 1000 h exposures of as-cast material at 700°C [36]. These observations suggest that a $D8_b$ phase-field spans the compositional range between the $Al_{0.3}$ and $Al_{1.0}$ alloys, though further investigations are necessary to establish the composition and temperature range in which the $D8_b$ phase forms. A few studies have also reported an $L1_2$ phase following thermal exposures ≤ 700°C in the compositional range $0.12 \geq x \geq 0.7$ [15,19–21,35,37–39,59] but it remains to be determined whether this phase is thermodynamically stable in the $Al_{0.5}$ alloy.

1.4. AlCrFeCoNi

In the as-cast condition, the equiatomic AlCrFeCoNi alloy has a dendritic microstructure consisting of AlNi-rich B2 DR and CrFe-rich A2 ID [22,24,25,27,43,45,47,61]. Occasionally, the $L1_2$ phase has also been reported in as-cast [3,27] and as-deposited materials [44]. Some studies have also observed the A1 phase in the as-cast state [25,62,63], but it is more commonly observed following heat-treatment in the temperature range 600–1200°C [2,9,10,12,22,43,45–47,64,65]. A detailed understanding of A1 phase precipitation is derived from an investigation into the CrFe-rich A2 precipitates in the as-cast condition by Manzoni *et al.* [24]. Using Atom Probe Tomography (APT), nm-scale partitioning of Cr and Fe within the CrFe-rich regions was revealed. This was attributed to a decomposition into Cr and Fe-rich phases, a conclusion that is supported by a recent study by Panda *et al.* [47], which observed that a FeNi-rich A1 phase developed at the expense of the A2 phase in the temperature range 800–1100°C. Together these studies indicate that the A1 phase forms from the transformation of the A2 phase, which leaves an open question as to whether the A2 phase remains thermodynamically stable at lower temperatures. In the same 600 – 1200°C temperature range in which the A1 has been observed, CrFe-rich $D8_b$ precipitates have also been reported [9,12,22,36,43–47]. However, in some cases it is possible that the $D8_b$ phase formed during cooling. For example, Tang *et al.* [43] estimated that their specimen contained 11% $D8_b$ phase following heat-treatment at

1150°C, but the alloy was cooled slowly at 10°C/min, providing ample time for $D8_b$ phase formation.

Despite significant interest in the AlCrFeCoNi alloy, there have been limited attempts to establish the equilibrium phase constitution of the alloy at temperatures below 1000°C. A study by Wang *et al.* [9], acquired in-situ XRD data from as-cast specimens during short duration heat-treatments between 300 and 1100°C. At room temperature, only reflections consistent with a B2 phase were recorded (including a {100} superlattice reflection at ~31° 2θ in Fig. 4f). However, as the temperature was increased to 600°C and above, A1 reflections were also identified, as well as $D8_b$ phase reflections in the temperature range 600 – 900°C. Corresponding DSC of the as-cast material revealed two endothermic peaks at around 600°C and 960°C, which were attributed to the formation of A1 + $D8_b$ and the dissolution of $D8_b$, respectively. This was recently corroborated through a combination of DSC, XRD and electron microscopy by Strumza & Hayun [66]. These findings indicate that the A1 phase is stable at temperatures ≥ 600°C and that the $D8_b$ phase exists in an intermediate temperature range between 600 and 960°C. This fits well with other studies which have reported B2, A2, A1 and $D8_b$ phases following exposures at 950°C [45], 900°C [47], 850°C [45], 800°C [47,64], 700°C [36], and 600°C [22]. Furthermore, Munitz *et al.* [45] found no evidence of the $D8_b$ phase in a specimen exposed at 975°C for 3 h, which comprised B2, A2 and A1 phases. However, it should be considered that all of these studies used as-cast material and all, except [36,64], employed relatively short-duration heat-treatments of up to 20 h, which may not have been sufficient to generate microstructures that reflect the equilibrium phase stability. For example, it is not possible to determine whether the phases that were present in the as-cast material remained thermodynamically stable following subsequent thermal exposure, or persisted due to kinetic considerations. Furthermore, as mentioned previously, the as-cast material is likely to contain solidification-induced elemental segregation, which can alter the precipitation pathway.

1.5. Consolidation

To form an overall picture of phase stability in the $Al_xCrFeCoNi$ system, information provided in the literature across a range of Al concentrations and temperatures were collated and plotted onto a temperature-composition graph, displayed in Fig. 1. To allow comparisons with the equilibrium phase predictions, only studies in which the alloy processing was conducive to the formation of equilibrium phases at the specified exposure temperatures were included. For example, data from alloys in the as-cast condition and anomalous results reported following short-duration annealing and heat-treatment from the as-cast state were omitted. In certain studies, some phases were not conclusively identified, or appeared to have been misidentified. In these cases, where possible, the identity of the phases was determined either through direct reanalysis of the published data (such as the presence of superlattice peaks in XRD) or according to circumstantial information in the paper (usually elemental partitioning information). Misidentification of the B2 phase as A2 (for reasons discussed in Section 1.3) was the most common source of irregularity. References and details of the phases reported in each study surveyed are provided in Table A of the Supplementary Information for this paper. Phases which have been re-identified are duly noted.

Based on the assessment of the existing literature, it appears that the $Al_{0.5}$ alloy has a dendritic structure comprised of Al-depleted A1 DR and AlNi-rich B2 ID and may form $D8_b$ phase following heat-treatment at temperatures ≤800°C. The $Al_{1.0}$ alloy, on the other hand, has a complex dendritic microstructure with AlNi-rich B2 dendrites and CrFe-rich ID. In addition to the majority B2 phase, it is commonly reported to contain A2, A1 and $D8_b$ phases. However, most of the present knowledge of phase stability in these alloys is
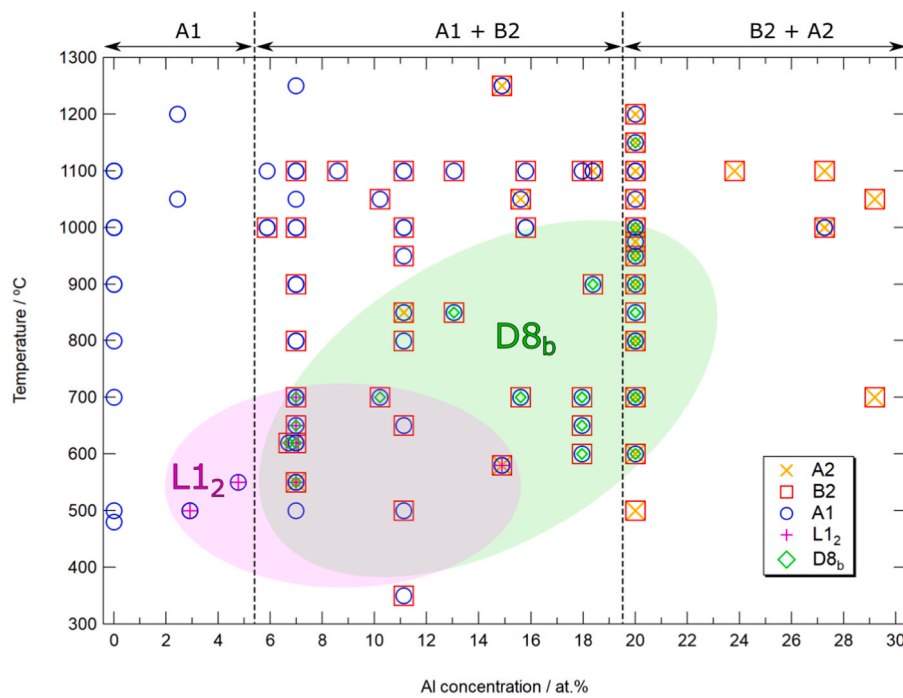
Fig. 1. Phases observed in Al$_x$CrFeCoNi alloys based on studies considered likely to encourage the formation of equilibrium phases. Blue circles indicate the observation of the A1 phase, while red squares, green diamonds, orange ×, and magenta + indicate the B2, D8$_b$, A2, and L1$_2$ phases, respectively. The dashed vertical lines denote the approximate minimum Al concentration for the formation of the B2 and A2 phases, as labelled above. The coloured ellipses highlight the approximate extent of the D8$_b$ and L1$_2$ phases. Further information on the experimental studies used to generate this plot is tabulated in the Supplementary information for this paper.

based upon studies that have applied relatively short-duration heat-treatments to as-cast materials. As such, the true equilibrium phase stability of these alloys remains uncertain. This is particularly true at temperatures below 1000°C, where the literature is sparse and longer-duration heat-treatments are necessary to compensate for the slower kinetics. As a result, the stability of the D8$_b$ phase, which can be highly deleterious to mechanical properties, remains poorly understood. A clear understanding of phase stability is essential for assessing the suitability of these alloys for structural applications at elevated temperatures. Therefore, the present work seeks to reliably establish the phase stability of the AlCrFeCoNi and Al$_{0.5}$CrFeCoNi alloys between 700 and 1000°C. To achieve this, specimens were subjected to a 72 h homogenisation heat-treatment at 1200°C, to remove any solidification-induced elemental segregation, and subsequently exposed at 1000, 850 and 700°C for 1000 h, to encourage the formation of equilibrium phases.

2. Experimental methods

50 g ingots of Al$_x$CrFeCoNi, where the nominal atomic ratio, $x = 0.5$ and 1.0 (equivalent to 11.1 and 20.0 at.% Al, respectively), were fabricated via arc melting of pure elemental metals, with purities ≥ 99.5%, under an inert Ar atmosphere. To improve the macroscopic homogeneity of the as-cast material, each ingot was inverted and re-melted five times.

Differential scanning calorimetry (DSC) was performed using a 'Netzsch 404 C' calorimeter and alumina crucible, under flowing Ar and at a heating rate of 10°C min^{-1}, to establish the solidus temperatures of the as-cast material. Subsequent DSC investigations were also performed to determine phase transition temperatures using a platinum crucible in a 'Netzsch 404 F1 Pegasus' calorimeter operated at a heating rate of 20°C min^{-1}. To remove any casting induced segregation, the ingots were encapsulated in evacuated and argon back-filled quartz tubes and heat-treated for 72 h at 1200°C (which is the operational temperature limit of quartz glass). Following homogenisation heat-treatment, the ingots were

sectioned into ~10 mm lengths and re-encapsulated for long duration thermal exposures of 1000 h at temperatures of 700, 850 and 1000°C. In all cases, samples were water quenched following heat-treatment to minimise any microstructural changes during cooling.

The microstructures of the homogenised and long duration exposed samples were characterised using back-scattered electron (BSE) imaging and energy dispersive X-ray spectroscopy (EDX) using an FEI 'NanoSEM 450' fitted with a Bruker 'xFlash 100' EDX detector. Additional BSE images and corresponding EDX data, including all quantitative measurements, were acquired using a 'Zeiss Gemini 300' SEM fitted with an Oxford Instruments 'X-MaxN' 50 mm^2 silicon drift EDX detector. Both microscopes were operated at 15 kV. The macroscopic composition of each ingot was determined by averaging the results of six or more large area (at least 500 × 500 μm) EDX measurements, whilst phase compositions were obtained from the average of at least ten point measurements. The error was calculated from the standard deviation of the measurements. X-ray diffraction data were acquired between angles of 20 and 100° 2θ using Ni-filtered Cu radiation in a Bruker D8 diffractometer. Crystal structures were identified from the diffraction data and their lattice parameters were determined by full pattern refinement using the Pawley method in Topas-Academic. Thermodynamic calculations for each alloy were performed using Thermo-Calc Software and the TCHEA4 database.

3. Results

Bulk alloy compositions obtained from each alloy in the homogenised condition are displayed in Table 2. The measured elemental concentrations closely matched the nominal alloy composition, with a maximum difference of 0.3 at.%. DSC of the as-cast material, available in the supplementary information (Supplementary B), was used to determine the solidus temperatures, which were 1340 and 1350°C for the Al$_{0.5}$ and Al$_{1.0}$ alloys, respectively. Notably, the trace for the Al$_{1.0}$ alloy featured two endothermic events at ~560 and 920°C.

Table 2
Alloy compositions determined from large area SEM EDX analysis (at.%). Values of error are quoted as the standard deviation between measurements.

Alloy	Al	Cr	Fe	Co	Ni
Al$_{0.5}$CrFeCoNi	11.2 ± 0.1	22.5 ± 0.1	22.1 ± 0.2	22.2 ± 0.2	22.0 ± 0.2
AlCrFeCoNi	20.2 ± 0.2	20.0 ± 0.3	19.7 ± 0.3	20.0 ± 0.3	20.1 ± 0.3
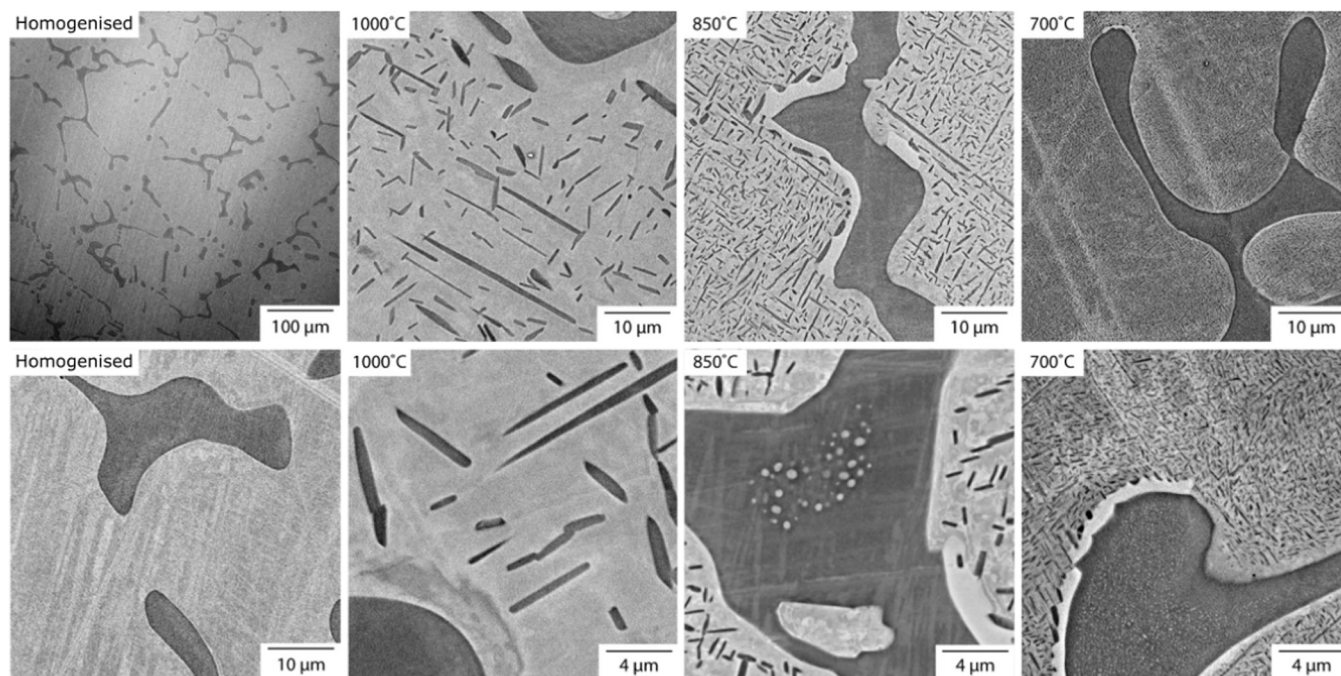
Fig. 2. BSE images of the Al$_{0.5}$CrFeCoNi alloy following homogenisation heat treatment at 1200°C for 72 h and after subsequent 1000 h exposures at 1000, 850 and 700°C. Low magnification (top) and higher magnification images (bottom) are included for each microstructural condition.

3.1. Al$_{0.5}$CrFeCoNi

Following homogenisation heat-treatment, the BSE images displayed in Fig. 2 showed that the Al$_{0.5}$ alloy had retained a dendritic microstructure, which comprised dark-contrast ID and light-contrast DR. The EDX elemental partitioning maps, displayed in Fig. 3, revealed that the ID were enriched in Al and Ni, and depleted of all other elements, while the DR showed a relative depletion of Al and Ni. Quantified compositions of each phase, provided in Table 3, showed that the DR was slightly depleted of Al and Ni, relative to the bulk alloy composition (Table 2). The ID, on the other hand, contained ~ 27 at.% Al ~31 at.% Ni, 18 at.% Co and less than 14 at.% Cr & Fe. However, closer inspection of the ID (Fig. 4), revealed that it contained a very fine-scale dispersion of light-contrast precipitates. The corresponding EDX partitioning maps showed that these precipitates were enriched in Cr and depleted in Al & Ni, relative to the ID phase. The fine-scale nature of these precipitates suggested that they had formed on cooling and, as such, were not representative of the equilibrium phase constitution at 1200°C. For this reason, they were not investigated further.

The homogenised material was subsequently heat-treated at 1000°C for 1000 h. In the resulting microstructure the dark-contrast ID remained and there was a proliferation of lath-like precipitates throughout the DR (Fig. 2). These lath-like precipitates had the same dark-contrast and elemental partitioning tendencies as the ID (Fig. 3). Moreover, the measured compositions, displayed in Table 3, were very similar, suggesting that they were another form of the same phase. The compositional data also revealed that the DR phase was significantly more depleted of Al and Ni than in the homogenised condition. This depletion of the DR phase corresponded to

an increase in the Al and Ni content of the ID phase and may also have been associated with an increase in the total volume fraction of the AlNi-rich phase.

Thermal exposure of the homogenised material at 850°C also resulted in the precipitation of dark-contrast lath-like precipitates (Fig. 2). These precipitates were much finer than in the 1000°C condition and appeared to have an orientation relationship with the DR phase. In addition, large, rounded light-contrast precipitates had formed along the boundary between the DR and ID. At the interface between this light-contrast phase and the DR matrix, the dark-contrast precipitates were substantially coarser than in the bulk. Small, spherical light-contrast precipitates were also observed within certain regions of the ID phase. The partitioning maps, displayed in Fig. 3 revealed that, as in the 1000°C condition, the dark-contrast ID phase and lath-like DR precipitates were enriched in Al & Ni and depleted of other elements relative to the DR. In contrast, the large, light-contrast precipitates on the DR/ID boundary were highly enriched in Cr, depleted of Al & Ni, and had an intermediate concentration of Fe & Ni relative to the DR and ID phases. It was also possible to observe that the small spherical precipitates within the ID were enriched in Cr and depleted of Al & Ni. The quantified phase compositions, displayed in Table 3, showed that the Al and Ni contents of the ID phase continued to increase with decreasing temperature. The reverse trend was observed for the DR matrix. The compositional data indicated that the dark-contrast lath-like DR precipitates had a very similar composition to that measured at 1000°C. However, there were significant errors associated with some of the elemental concentrations measured. This is likely to be caused by sampling of the surrounding DR phase during EDX point spectra collection, due to the small size of the precipitates. Lastly, the light-
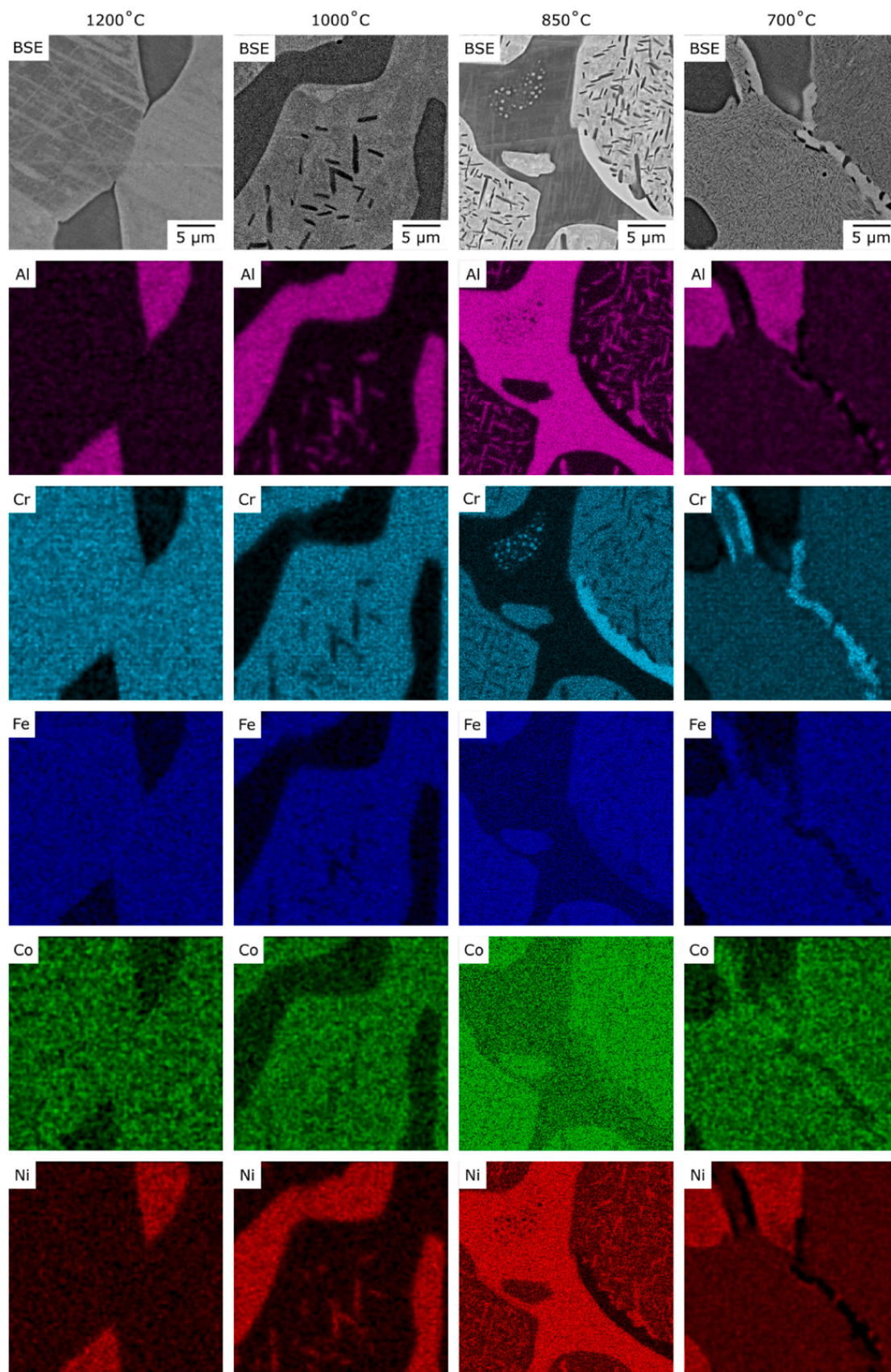
Fig. 3. BSE images (top) and EDX elemental maps (beneath) for $Al_{0.5}CrFeCoNi$ following homogenisation heat treatment at 1200°C for 72 h and following subsequent 1000 h exposures at 1000, 850 and 700°C.

Table 3

Crystallographic and compositional data (in at.%) for the phases observed in the $Al_{0.5}CrFeCoNi$ alloy in the homogenised condition and following subsequent 1000 h exposures at 1000, 850 and 700°C. DR and ID refer to the dendrite and interdendrite regions, respectively. To assist the reader in identifying the precipitate (ppt.) phases in the microstructure, the ppt. contrast under BSE imaging and its location (in the DR / ID or on the boundary between the DR and ID) is noted e.g. "light[-contrast] boundary ppt".

Condition	Phase / structure	a (Å)	c (Å)	Al	Cr	Fe	Co	Ni
1200°C	DR / A1	3.60	–	9.1 ± 0.1	24.0 ± 0.2	23.3 ± 0.2	22.9 ± 0.2	20.7 ± 0.2
	ID / B2	2.88	–	27.1 ± 0.6	10.8 ± 0.8	13.3 ± 0.3	17.8 ± 0.2	31.0 ± 0.5
1000°C	DR / A1	3.60	–	6.1 ± 0.1	26.3 ± 0.3	24.9 ± 0.3	23.9 ± 0.2	18.7 ± 0.4
	ID / B2	2.88	–	32.0 ± 0.1	6.4 ± 0.2	10.5 ± 0.2	15.8 ± 0.2	35.3 ± 0.2
	dark DR ppt. / B2	2.88	–	30.2 ± 1.9	8.5 ± 1.9	11.5 ± 1.1	16.1 ± 0.6	33.7 ± 1.7
850°C	DR / A1	3.59	–	3.9 ± 0.2	27.2 ± 0.7	26.4 ± 0.3	25.1 ± 0.3	17.4 ± 0.5
	ID / B2	2.88	–	34.0 ± 0.2	4.4 ± 0.2	9.6 ± 0.1	14.4 ± 0.2	37.6 ± 0.3
	dark DR ppt. / B2	2.88	–	30.9 ± 2.6	7.7 ± 2.8	11.1 ± 1.7	15.0 ± 1.0	35.3 ± 2.7
	light boundary ppt. / D8$_b$	8.80	4.54	1.0 ± 0.2	51.5 ± 0.7	21.1 ± 0.2	19.9 ± 0.1	6.5 ± 0.4
700°C	DR / A1	3.58	–	8.2 ± 2.3	20.5 ± 2.5	24.5 ± 1.5	25.8 ± 0.6	21.0 ± 2.2
	ID / B2	2.88	–	32.2 ± 1.3	5.6 ± 1.2	11.1 ± 0.5	15.8 ± 0.6	35.3 ± 1.4
	dark DR ppt. / B2	2.88	–	25.6 ± 3.4	11.2 ± 3.2	13.7 ± 1.9	17.1 ± 1.2	32.4 ± 2.7
	light boundary ppt. / D8$_b$	–	–	1.4 ± 0.6	50.5 ± 1.3	20.4 ± 0.4	21.9 ± 0.2	5.8 ± 0.9

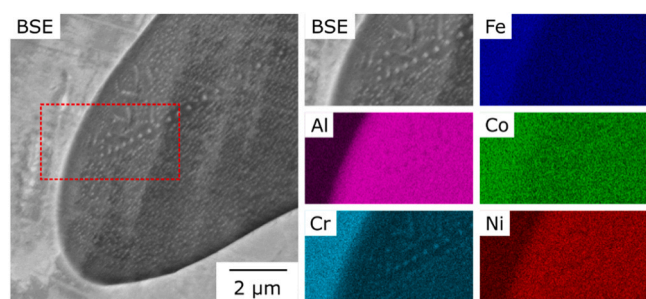**Fig. 4.** BSE image showing fine-scale light-contrast precipitates within the ID of the $Al_{0.5}CrFeCoNi$ alloy following homogenisation heat treatment at 1200°C for 72 h. Adjacent EDX maps, acquired from the region identified by the red dashed box in the large BSE image, reveal elemental partitioning within the ID.

contrast boundary phase contained ~ 52 at.% Cr and was highly depleted of Al and Ni, which had concentrations ~ 1 and 7 at.%, respectively.

Heat-treatment at 700°C resulted in the precipitation of fine-scale, dark-contrast lath-like precipitates throughout the DR, as well as the formation of rounded light-contrast precipitates along the boundaries between the DR grains and along the interface between the DR and ID. As with the previous condition, the dark-contrast precipitates, which formed at the interface between the DR and the light-contrast phase, were significantly coarser than those in the bulk. Additionally, the high-resolution image, displayed in Fig. 2, revealed a proliferation of very fine-scale light-contrast precipitates throughout the ID. These precipitates were much finer but had a similar morphology to those observed in the 850°C condition, which were enriched in Cr and depleted of Al and Ni (Fig. 3). The elemental partitioning maps, corresponding to the high-resolution image of the 700°C condition (Fig. 3), indicated that the light-contrast boundary precipitates were enriched in Cr and depleted of all other elements relative to the DR matrix. They also revealed that the coarser dark-contrast precipitates, which formed adjacent to the light-contrast phase, were enriched in Al & Ni and depleted of Co. Higher resolution partitioning maps, included in the supplementary information for this paper (Supplementary C), also showed that the finer dark-contrast precipitates in the DR were enriched in Al & Ni and depleted of all other elements relative to the DR matrix. The maps also revealed the presence of a Cr-rich and AlNi-depleted phase, which was co-located with dark-contrast precipitates in the DR. The compositional data, Table 3, revealed that the DR matrix contained substantially more Al & Ni and less Cr than in the 850°C condition. The Al & Ni concentration in the ID phase was also higher than in the 850°C condition, which was compositionally more

similar to the ID phase in the 1000°C condition. However, the composition of the light-contrast boundary phase closely matched that measured in the 850°C specimen. Quantified compositional data from the dark-contrast DR precipitates should be treated with caution as the precipitates were even smaller than in the 850°C condition. Nevertheless, the measured composition was within the error of the compositions quoted for the 1000 and 850°C conditions. As in the 850°C condition, the fine-scale nature of the light-contrast ID precipitates prevented the acquisition of reliable compositional data. The Cr-rich DR precipitates (Supplementary C) were also too fine for their compositions to be quantified using SEM-EDX.

The XRD data obtained from the $Al_{0.5}$ alloy following exposure at each heat-treatment temperature are displayed in Fig. 5. In each condition, the XRD patterns included reflections corresponding to an A1 and a B2 phase. In the homogenised condition, the reflections of greatest intensity belonged to the A1 phase, which had a lattice parameter of 3.60 Å. The remaining reflections corresponded to a B2 phase with a lattice parameter of 2.88 Å. The B2 lattice was identified based on the {100} superlattice peak at ~ 31° 2θ, which distinguishes the B2 structure from the A2 structure. Based on previous observations of a AlNi-rich B2 phase in this system [9,30,47,48,56], it was determined that the DR phase was A1 and the ID were B2. Following heat-treatment at 1000°C, the reflections corresponding to the B2 phase were more intense, revealing a second superlattice reflection, the {111}, at ~ 55° 2θ. In addition, a slight shoulder was noticed on the lower 2θ side of the A1 {022} peak at ~74° 2θ, which is thought to be due to the presence of a third, weak B2 {012} superlattice reflection. In the absence of any reflections corresponding to additional phases in the XRD pattern, it was straightforward to conclude that the AlNi-rich lath-like precipitates that formed within the A1 DR phase were B2. In the 850°C condition, the XRD pattern closely resembled that of the 1000°C specimen, apart from the appearance of five low intensity reflections between 42 and 50° 2θ. These reflections, which are characteristic of the D8$_b$ phase [9,10,22,41,42,44,45,47], were attributed to the Cr-rich light-contrast phase that appeared on the DR/ID boundaries at this temperature. At the lowest exposure temperature of 700°C, the XRD pattern also resembled that of the 1000 and 850°C specimens. However, despite the presence of Cr-rich precipitates in the microstructure, there was no clear evidence of D8$_b$ phase reflections in the angular range 42–50° 2θ (although some deviation from the baseline is noticeable between 46 and 49° 2θ). This is likely to be because the precipitates that formed on the DR/ID boundaries at 700°C were smaller and appeared to occupy a smaller volume fraction than at 850°C (Fig. 2), so the diffracted signal intensity originating from them is likely to have been lower. Furthermore, the Cr-rich precipitates that formed within the DR (Supplementary C), were unlikely to have produced a sharp diffraction peak due to their < 200 nm crystallite size [67].
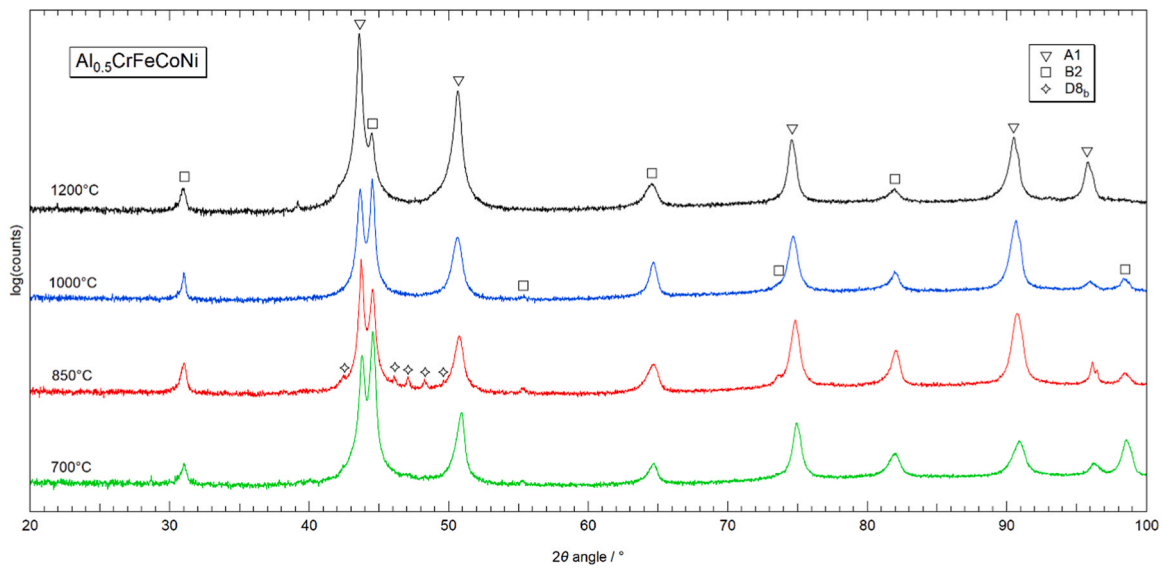
Fig. 5. X-ray diffraction patterns from Al$_{0.5}$CrFeCoNi following homogenisation heat treatment at 1200°C for 72 h and after subsequent 1000 h exposures at 1000, 850 and 700°C. The lattice parameters for each phase are provided in Table 3.

3.2. AlCrFeCoNi

BSE images of the Al$_{1.0}$ alloy in the homogenised and heat-treated conditions are displayed in Fig. 6. The homogenised material had a dendritic microstructure consisting of dark-contrast DR, which contained a very fine dispersion of light-contrast precipitates and light-contrast ID, which contained much coarser dark-contrast precipitates. In addition, certain regions of the ID contained another light-contrast phase. This phase was usually found on the grain boundaries, as observed in the BSE image in Fig. 7. The image also reveals the presence of some discrete light-contrast DR precipitates that were significantly coarser than the surrounding fine-scale precipitates. It should also be noted that the ID matrix had a bimodal contrast in the BSE images (Fig. 6). However, point EDX spectra

showed that there was no difference in composition between these lighter and darker contrast regions. As such, the change in contrast is attributed to a difference in crystallographic orientation and associated electron channelling contrast. The elemental partitioning maps, displayed in Fig. 7, showed that the DR was rich in Al and Ni and depleted of Cr and Fe. Conversely, the ID matrix was enriched in Cr & Fe and were depleted of Al & Ni. Co appeared to be evenly distributed throughout the microstructure. The dark-contrast precipitates within the ID exhibited the same elemental partitioning tendencies as the dendritic material. The partitioning of the light-contrast ID phase, which appeared along the grain boundaries, was very similar to the ID matrix, making it difficult to distinguish between the two phases. However, the Cr partitioning map did show that the light-contrast boundary phase was slightly less enriched in
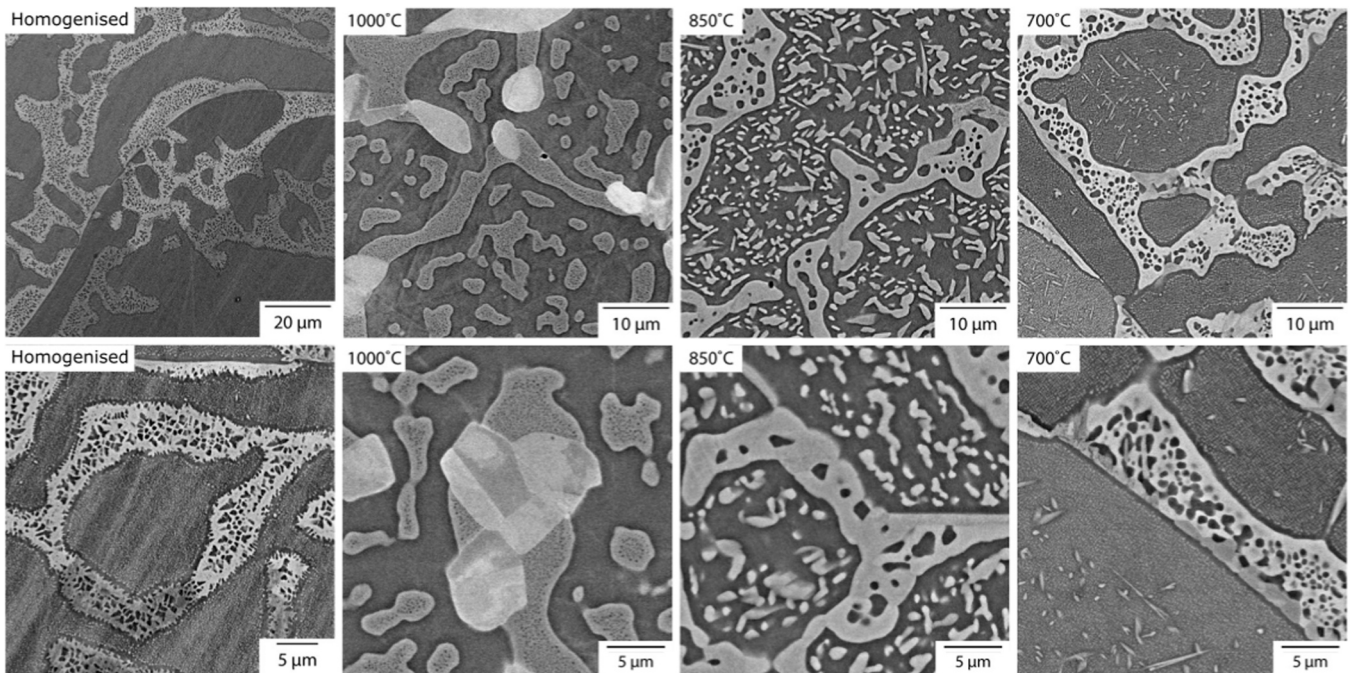

Fig. 6. BSE images of the AlCrFeCoNi alloy following homogenisation heat treatment at 1200°C for 72 h and after subsequent 1000 h exposures at 1000, 850 and 700°C. Low magnification (top) and higher magnification images (bottom) are included for each microstructural condition.
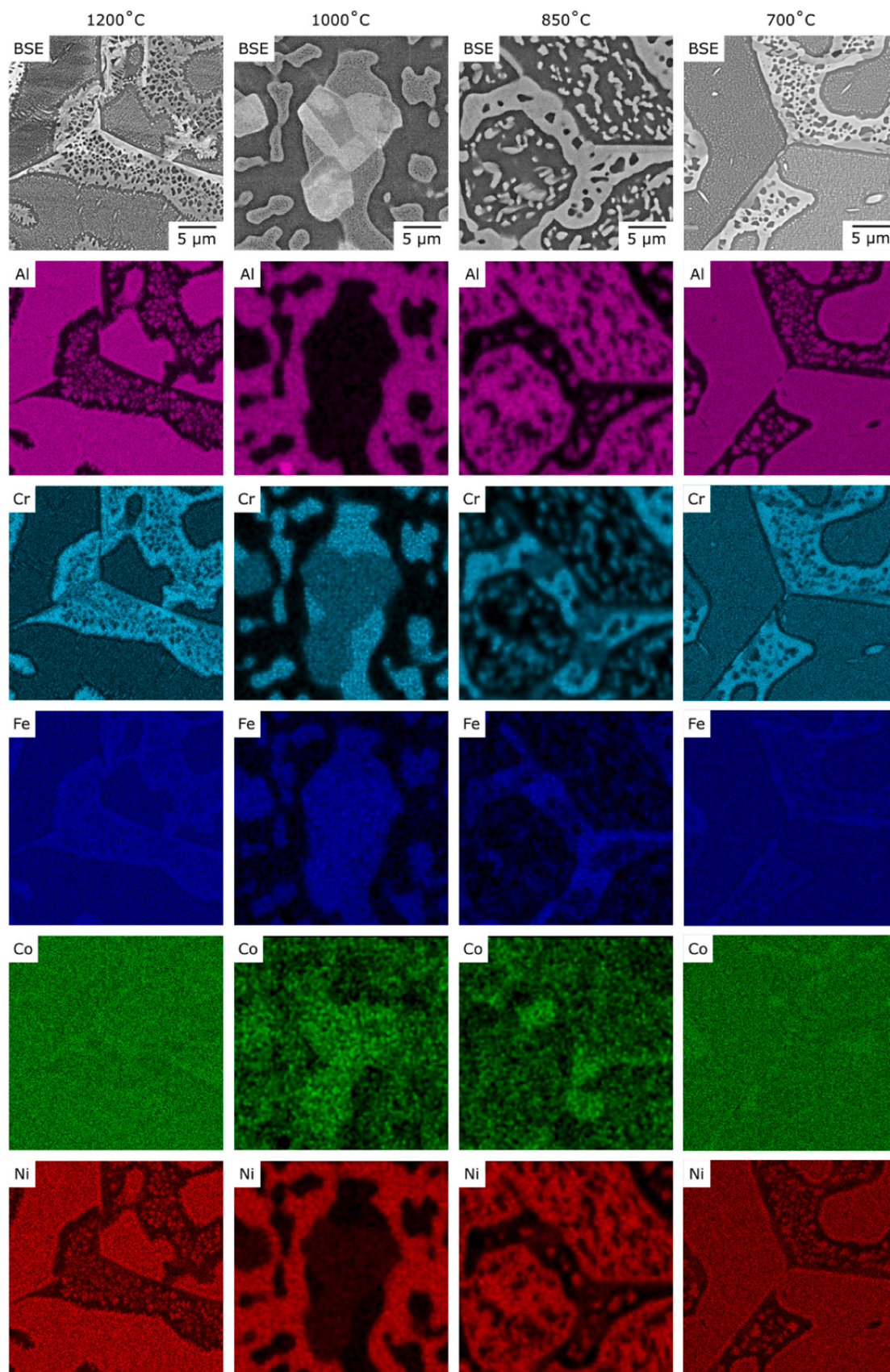
Fig. 7. BSE images (top) and EDX elemental maps (beneath) for AlCrFeCoNi following homogenisation heat treatment at 1200°C for 72 h and after subsequent 1000 h exposures at 1000, 850 and 700°C.

Table 4

Crystallographic and compositional data (in at.%) for the phases observed in the AlCrFeCoNi alloy in the homogenised condition and following subsequent 1000 h exposures at 1000, 850 and 700°C. DR and ID refer to the dendrite and interdendrite regions, respectively. To assist the reader in identifying the precipitate (ppt.) phases in the microstructure, the ppt. contrast under BSE imaging and its location (in the DR or ID) is noted. Phases denoted with an asterisk are not thought to be stable at the exposure temperature.

Condition	Phase / structure	a (Å)	c (Å)	Al	Cr	Fe	Co	Ni
1200°C	DR / B2	2.88	–	26.6 ± 1.1	12.0 ± 1.6	15.9 ± 0.7	20.0 ± 0.2	25.5 ± 1.2
	ID / A2	2.88	–	3.6 ± 0.7	39.6 ± 1.1	29.9 ± 0.5	20.4 ± 0.2	6.5 ± 0.8
	dark ID ppt. / B2	2.90	–	23.1 ± 1.9	16.6 ± 3.2	18.1 ± 1.6	19.9 ± 0.3	22.3 ± 2.5
	light ID ppt. / A1	–	–	5.9 ± 0.9	29.6 ± 1.7	29.7 ± 0.6	23.6 ± 0.7	11.2 ± 0.8
	light DR ppt. / D8$_b$*	8.79	4.56	–	–	–	–	–
1000°C	DR / B2	2.88	–	31.5 ± 0.4	8.1 ± 0.6	13.0 ± 0.2	19.3 ± 0.1	28.1 ± 0.4
	ID / A2	2.87	–	5.5 ± 1.1	41.2 ± 1.2	27.9 ± 0.8	18.6 ± 0.3	6.8 ± 1.1
	dark ID ppt. / B2	2.89	–	–	–	–	–	–
	light DR ppt. / A2	2.87		5.9 ± 1.4	40.3 ± 1.7	27.7 ± 1.1	18.8 ± 0.2	7.3 ± 1.4
	light ID ppt. / A1	3.60	–	5.8 ± 0.1	27.6 ± 0.2	30.0 ± 0.2	24.0 ± 0.2	12.6 ± 0.2
850°C	DR / B2	2.88	–	33.3 ± 0.2	4.9 ± 0.2	12.7 ± 0.1	19.4 ± 0.2	29.7 ± 0.2
	ID / D8$_b$	8.78	4.56	1.4 ± 0.2	47.6 ± 0.6	27.6 ± 0.2	18.9 ± 0.2	4.5 ± 0.2
	dark ID ppt. / B2	2.89	–	33.0 ± 0.7	5.5 ± 1.1	13.0 ± 0.4	19.3 ± 0.2	29.2 ± 0.7
	light ID ppt. / A1	3.59	–	3.7 ± 0.1	25.3 ± 0.3	34.5 ± 0.2	25.2 ± 0.2	11.3 ± 0.2
	light DR ppt. / D8$_b$	8.79	4.56	1.8 ± 0.6	46.9 ± 1.1	27.5 ± 0.2	19.1 ± 0.2	4.7 ± 0.6
700°C	DR / B2	2.88	–	29.9 ± 0.9	7.7 ± 1.7	15.2 ± 0.6	19.7 ± 0.4	27.5 ± 1.2
	ID / D8$_b$	8.78	4.55	1.5 ± 0.9	47.0 ± 1.7	27.2 ± 0.4	19.9 ± 0.2	4.4 ± 1.0
	dark ID ppt. / B2	2.89	–	28.5 ± 2.8	10.2 ± 3.9	15.6 ± 1.8	19.4 ± 0.7	26.3 ± 2.5
	light ID ppt. / A1	3.58	–	2.2 ± 0.2	23.2 ± 0.2	36.7 ± 0.4	27.2 ± 0.3	10.7 ± 0.2
	light DR ppt. / D8$_b$	8.78	4.55	–	–	–	–	–

Cr. The partitioning maps also showed that the light-contrast DR precipitates were enriched in Cr & Fe and depleted of Al and Ni, relative to the surrounding DR matrix. Compositional data from the DR matrix was determined from the precipitate-free zone around the ID. The quantified composition, displayed in Table 4, showed that the DR matrix phase was enriched in Al & Ni and depleted of Cr & Fe, relative to the bulk alloy composition. The ID matrix, on the other hand, contained ~ 40 at.% Cr, ~ 30 at.% Fe and only around 5 at.% of Al and Ni. The dark-contrast precipitates within the ID had a similar composition to the DR matrix phase. The compositional data also showed that the light-contrast ID boundary phase contained significantly less Cr (~ 30 at.%) and more Ni, Al and Co than the ID matrix.

Following heat-treatment at 1000°C, the BSE images (Fig. 6) showed that the specimen had retained its dendritic structure, comprising a dark-contrast DR phase and light-contrast ID phase. However, instead of the fine dispersion of light-contrast precipitates seen in the homogenised condition, the DR contained large, light-contrast precipitates, which were very similar in appearance to the ID regions, both of which contained fine-scale dark-contrast precipitates. Additional large precipitates also formed in the ID, which were lighter in contrast than the ID matrix and did not contain any secondary precipitates. These light-contrast precipitates sometimes featured regions of different contrast, as seen in the higher magnification image in Fig. 6, which may be due to the presence of grain or twin boundaries. Elemental partitioning maps, corresponding to the higher magnification image, are displayed in Fig. 7. These revealed that, as in the homogenised condition, Al and Ni partitioned strongly to the DR and Cr and Fe to the ID. The light-contrast precipitates in the DR exhibited the same elemental partitioning as the ID, which suggested that they were another instance of the same phase. Cr and Fe also partitioned to the light-contrast ID precipitates, though it was clear that they had a lower concentration of Cr than the surrounding ID. The light-contrast phase also appeared to have a greater concentration of Co than the ID. Indeed, the phase compositions in Table 4 showed that the concentration of Co was ~ 24 at.% in the light-contrast ID precipitates, compared with ~ 19 at.% in the ID and DR. The compositional analysis also confirmed that the light-contrast ID precipitates were enriched in Cr and Fe relative to the bulk composition but depleted of Al and Ni. In fact, their composition was very similar to that of the light-contrast ID precipitates measured in the homogenised condition. The composition of the ID was also very similar to that measured in the homogenised condition. In contrast,

the DR was more enriched in Al and Ni and contained lower concentrations of Cr and Fe. It should be noted that, due to their fine scale, it was not possible to separate the EDX signals of the dark-contrast secondary precipitates from that of the ID matrix and light-contrast DR precipitates in which they appeared. As such, the elemental composition quoted for these regions includes both phases.

In the 850°C condition, the BSE images displayed in Fig. 6 revealed extensive precipitation in both the DR and ID. Large, light-contrast precipitates were observed throughout the DR and dark-contrast precipitates, of a similar size, were present within the ID. Furthermore, aside from the dark-contrast precipitates, the ID had a bimodal contrast, which suggested the presence of an additional light-contrast phase, as was observed in the homogenised and 1000°C conditions. This was confirmed by the elemental partitioning maps (Fig. 7), which revealed differential partitioning within the light-contrast areas of the ID. Some regions were highly enriched in Cr and depleted of all other elements, while other regions were enriched in Fe and had an intermediate Cr content, more similar to the light-contrast ID phase observed in the homogenised and 1000°C conditions. It is also worth noting that, in certain regions (Fig. 7), the three ID phases were observed to coexist in contact. The partitioning maps also showed that the light-contrast DR precipitates exhibited the same elemental partitioning as the Cr-rich regions of the ID. Additionally, the dark-contrast ID precipitates exhibited the same elemental partitioning as the DR matrix phase. Indeed, the quantified compositions (Table 4) revealed that there was no significant difference in composition between these phases. Higher-resolution EDX maps (Supplementary D), also revealed the formation of another dark-contrast phase within the Fe-rich regions of the ID. This phase was enriched in Cr and C, so it is believed to be a Cr-based carbide phase, such as $M_{23}C_6$, which has previously been reported in alloys of this system due to the unintentional incorporation of C [32,68–71].

The microstructure that developed at 700°C was similar to that observed at 850°C. In both, the dark-contrast DR contained light-contrast precipitates and light-contrast ID contained dark-contrast precipitates. Furthermore, the elemental partitioning maps (Fig. 7) showed that the ID in the 700°C microstructure were also comprised of two light-contrast phases, which were easily distinguished by the partitioning of Cr to one and Fe & Co to the other. Furthermore, the FeCo-rich ID phase was again found to contain fine-scale secondary dark-contrast precipitates. However, the light-contrast precipitates that formed within the DR were much finer than in the 850°C
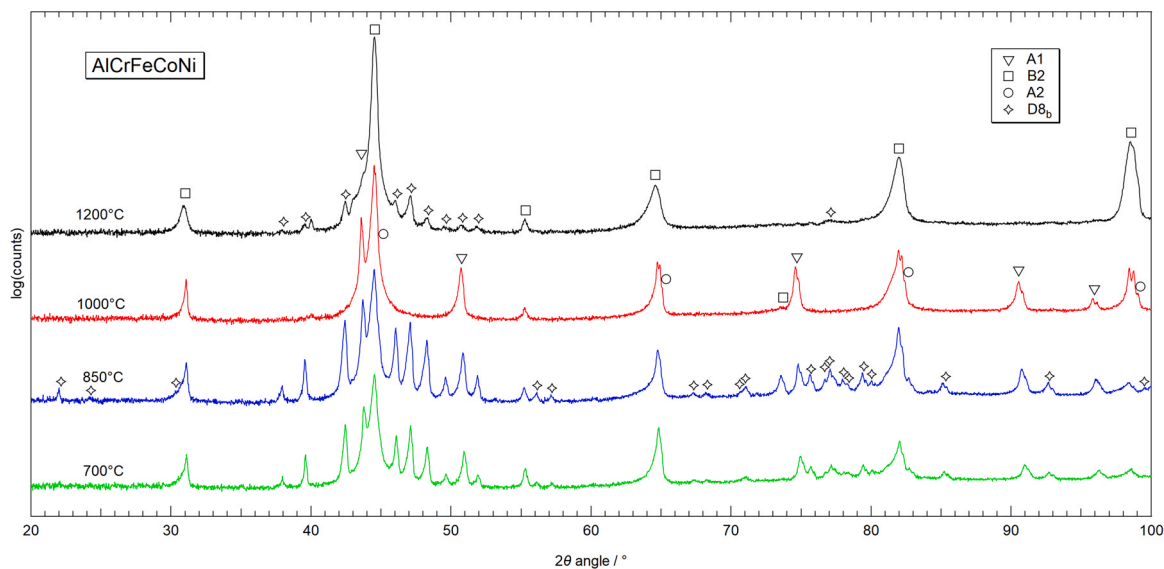
Fig. 8. X-ray diffraction patterns from AlCrFeCoNi following homogenisation heat treatment at 1200°C for 72 h and after subsequent 1000 h exposures at 1000, 850 and 700°C. The lattice parameters for each phase are provided in Table 4.

condition and had two distinct morphologies: (i) uniformly dispersed ultra-fine-scale spherical precipitates, similar to those observed in the homogenised condition, and (ii) coarser lath-like precipitates. The elemental partitioning maps showed that the coarser of these precipitates were Cr-rich and AlNi-depleted, exhibiting the same elemental partitioning behaviour as the Cr-rich ID precipitates. Furthermore, higher resolution EDX maps, included in the supplementary information (Supplementary D) revealed that the finer-scale DR precipitates were also enriched in Cr and depleted of Al and Ni relative to the surrounding DR matrix. The EDX maps also showed that, as in the 850°C condition, the dark-contrast secondary precipitates in the ID were enriched in Cr and C (thought to have been introduced during manufacture), indicating that they were likely to be a Cr-carbide phase. Unfortunately, it was not possible to obtain reliable compositional information from these, or the light-contrast DR precipitates, due to their small size. The compositions measured for the other phases (Table 4) were similar to those measured in the 850°C specimen. The compositional data also revealed that there was no significant compositional difference between dark-contrast precipitates in the ID and the DR matrix phase (measured in the precipitate-free regions around the DR/ID boundaries).

The XRD patterns of the homogenised and heat-treated conditions are displayed in Fig. 8. For the homogenised material, reflections corresponding to a B2 phase and a D8$_b$ phase were initially identified, with lattice parameters of 2.88 and 8.79, 4.56 Å, respectively. After heat-treatment at 1000°C, the reflections corresponding to the B2 phase remained and additional reflections belonging to an A1 phase with a lattice parameter of 3.60 Å also appeared, but there was no evidence of the D8$_b$ phase. The 850 and 700°C specimens, on the other hand, exhibited reflections corresponding to the B2, A1 and D8$_b$ phases, the lattice parameters for which are provided in Table 4. However, closer inspection of the B2 peaks in each condition revealed that each one possessed significant asymmetry. This was most clearly observed in the 1000°C pattern, where all the B2 peaks were skewed to the lower 2θ side, whilst certain peaks also had shoulders on the higher 2θ side. These asymmetries in the B2 peak shape were indicative of a superposition of multiple reflections, which suggested that the specimens contained additional phases. The fits obtained for the XRD patterns of the homogenised and 1000°C specimens, using a Pawley fitting procedure, are displayed in Figs. 9 and 10, respectively. The coloured markers beneath show the

position of the significant reflections from each phase. As can be seen in the inset of the 1000°C pattern (Fig. 10), fitting three peaks to the peak at ~ 82° showed that the lower 2θ skew could be accounted for by a broad peak and the higher 2θ shoulder by a sharp peak, with noticeable splitting of the Kα$_1$ / Kα$_2$ signals. Since the lower 2θ skew was present on every B2 peak, the broad peak must correspond to a secondary B2 phase with a slightly larger lattice parameter of 2.89 Å. However, the higher 2θ shoulder was only present on the fundamental B2 reflections and was not observed on the B2 superlattice reflections. This suggested that the sharper peaks belonged to an A2 phase with a slightly smaller lattice parameter of 2.87 Å. These small differences in lattice parameter between the two B2 phases and the A2 phase can be attributed to differences in composition [67]. The difference in peak breadth, on the other hand, is likely to be associated with broadening caused by a very small crystallite size [67]. Accordingly, the broad peaks are thought to originate from a phase comprised of fine-scale precipitates or very small grains.

Based on the evidence presented above, it was possible to establish with a reasonable degree of confidence, which phases identified in the microstructure corresponded to the structures identified in the XRD data. For the homogenised alloy: the B2 phase, which had the most intense reflections in the XRD pattern (Fig. 9), is likely to be the AlNi-rich DR phase as Al and Ni are known to partition to the B2 [9,30,47,48,56]. The ID, on the other hand, were enriched in Cr and Fe, so are likely to take the A2 structure, which was identified by XRD as the sharp peaks on the higher 2θ shoulder of the B2 peaks (Fig. 9). The close correspondence in composition between the dark-contrast ID precipitates and the DR suggested that they were also B2 phase. With this in mind, it should be noted that the slightly higher Cr & Fe concentrations (and correspondingly lower concentrations of Al & Ni) in the small ID precipitates may be due to sampling of the surrounding ID phase during EDX acquisition. Based on the small size of these B2 precipitates, it was also concluded that they were responsible for the broad B2 reflections, which had a slightly larger lattice parameter than the reflections belonging to the DR B2 phase (resulting in the lower 2θ skew on the B2 peaks). The D8$_b$ phase reflections identified in the XRD data were attributed to the coarser light-contrast precipitates, which formed in the DR (the fine-scale DR precipitates are considered at the end of this section). Because of the small volume fraction of the light-contrast ID boundary phase, corresponding XRD reflections were not clearly visible. Fortunately, however, in the 1000°C condition, light-contrast ID precipitates,
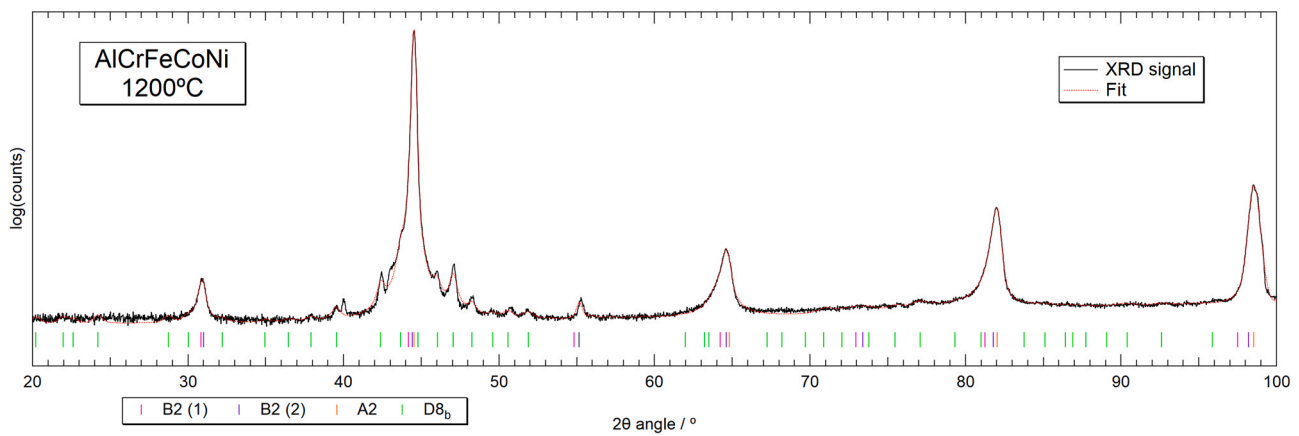
Fig. 9. X-ray diffraction pattern from AlCrFeCoNi in the homogenised (1200°C for 72 h) condition. The red dashed line shows the overall fit obtained using a Pawley refinement in TOPAS and the coloured markers beneath show the position of the significant reflections of each phase included in the fitting procedure. The lattice parameters for each phase are provided in Table 4.

which that had the same composition as those measured in the homogenised condition (Table 4), were much larger and strong A1 reflections were observed in the XRD pattern. This indicated that the light-contrast ID boundary phase observed in the homogenised condition was the A1 phase. Indeed, on closer inspection of the XRD pattern obtained from the homogenised material, a slight shoulder can be seen on the lower 2θ side of the B2 reflection at ~44°, where the A1 {111} reflection is expected. In the 1000°C specimen, the sharp B2 and A2 reflections (Fig. 10) were also attributed to the AlNi-rich B2 DR matrix and CrFe-rich A2 ID matrix, respectively. The fine-scale dark-contrast precipitates, contained within the ID, were also assigned the B2 structure, and corresponded to the broad B2 reflections. Furthermore, as discussed above, the A1 reflections were attributed to the light-contrast precipitates, enriched in Cr, Fe and Co, which formed from the ID. At 850°C, it was clear from the XRD data (Fig. 8) and the elemental partitioning of Al and Ni (Fig. 7) that the DR maintained a B2 structure. Conversely, the light-contrast DR precipitates were enriched in Cr and Fe and highly depleted of Al and Ni. Since the proliferation of this light-contrast DR phase coincided with the emergence of intense D8$_b$ phase reflections in the XRD pattern, it was logical to conclude that it was the D8$_b$ phase. The D8$_b$ phase was also significantly more enriched in Cr and slightly more depleted of Al & Ni than the A2 phase that appeared at higher temperatures. The ID comprised two light-contrast phases that were Cr and FeCo-rich, respectively (Fig. 7). It also contained smaller, dark-contrast precipitates, which were assigned, as previously, to the broad B2 reflections identified in the XRD data. Of the two light-contrast phases in the ID, one had the same composition as the light-contrast DR precipitates, so was also assigned the D8$_b$ phase. The other light-contrast phase in the ID closely matched the composition of the A1 phase in the 1000°C microstructure. The XRD data obtained from the 700°C specimen was very similar to that of the 850°C specimen. There was also a close correspondence between the microstructures and phase compositions. As such, it was determined that the DR were B2 and contained small lath-like D8$_b$ precipitates, similar to those identified in the homogenised condition. The ID, on the other hand, were comprised of two light-contrast phases, the D8$_b$ and A1, along with smaller dark-contrast B2 precipitates. In both the homogenised and 700°C conditions, an ultra-fine dispersion of light-contrast, Cr-rich & AlNi-depleted precipitates were also present throughout the DR regions. These precipitates were around 10 nm in diameter and had a spherical or cuboidal morphology, which indicated that they were coherent with the B2 matrix. Furthermore, no additional XRD reflections, which might originate from these precipitates, were observed. As such, the fine-scale DR precipitates are thought to take the A2 structure, which is coherent with the B2 structure. Reflections originating from these precipitates were not observed in the XRD patterns due to the peak broadening associated with their very small crystallite size and the fact that their reflections coincide with much more intense B2 / A2 reflections.
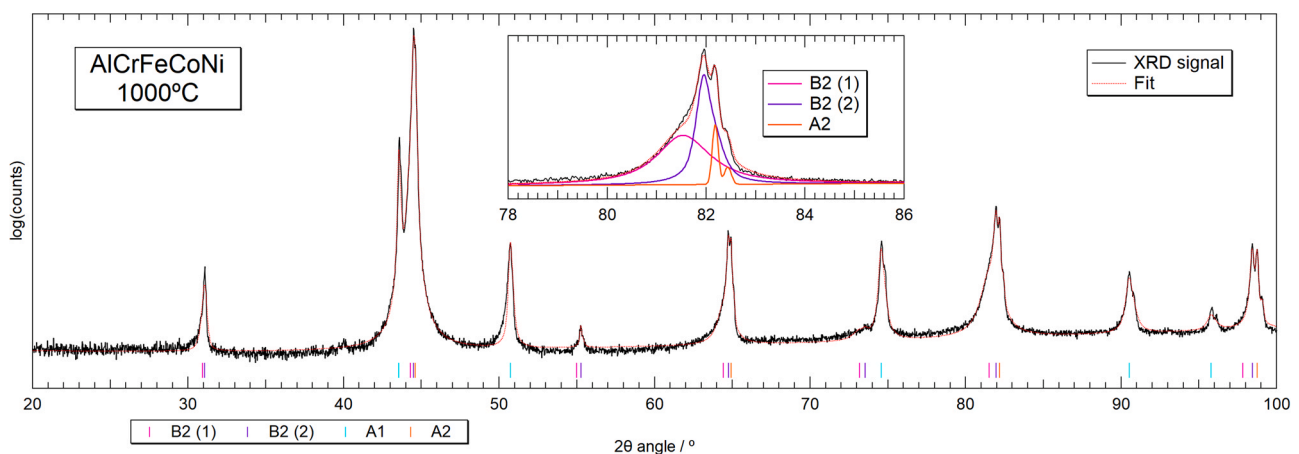

Fig. 10. X-ray diffraction pattern from AlCrFeCoNi in the 1000°C/1000 h heat-treated condition. The red dashed line shows the overall fit obtained using a Pawley refinement in TOPAS and the coloured markers beneath show the position of the significant reflections of each phase included in the fitting procedure. The figure inset above the spectrum is an enlarged view of the peak at ~ 82° 2θ and the fitted reflections that are attributed to two B2 phases and an A2 phase, which give rise to the overall peak shape. The lattice parameters for each phase are provided in Table 4.

4. Discussion

4.1. Effect of Al on phase stability

Building on extensive literature data, the results presented here help to establish the equilibrium phase stability of the $Al_xCrFeCoNi$ system. In the homogenised condition (1200°C) and following heat-treatment at 1000°C, the $Al_{0.5}$ alloy had a dual phase dendritic microstructure comprised of A1 DR and B2 ID. However, following heat-treatment at 850°C and 700°C, $D8_b$ phase precipitates developed at the DR/ID boundaries, confirming the existence of a $D8_b$ phase field spanning between the $Al_{0.3}$ and $Al_{1.0}$ alloys. This supports the findings of Butler and Weaver [36], who identified the $D8_b$ phase along the DR/ID boundary, following exposure of as-cast $Al_{0.45}$ (10 at. % Al) material at 700°C for 1000 h. The composition of the $D8_b$ phase, measured by STEM-EDX, also closely matched the composition measured in this study (Table 3). XRD reflections, characteristic of the $D8_b$ phase, have also previously been observed in the $Al_{0.6}$ alloy following heat-treatment of as-cast material at 850°C for 4 h [42]. In this case, the $D8_b$ precipitates were reported to contain a much lower concentration of Cr (27.5 at.%) and significantly higher concentrations of Al (7.9 at.%), Fe (29.4 at.%) and Ni (13.9 at.%), based on SEM-EDX analysis. These differences in elemental composition are probably due to the small size of the $D8_b$ precipitates analysed in [42], which appeared to be around 250 nm in diameter. At this scale, compositional analysis using SEM-based EDX is highly prone to errors as the EDX signal is generated from a much larger volume of the specimen.

The $Al_{1.0}$ alloy had a dendritic microstructure comprised of a B2 DR and an A2 + A1 ID in the homogenised condition. In addition, two fine-scale Cr-rich precipitate phases were present within the DR; nm-scale cuboidal A2 and coarser lath-like $D8_b$. Following exposure at 1000°C, B2, A2 and A1 phases were also present but there was no evidence of the $D8_b$ phase. However, at 850°C, the A2 phase was replaced by $D8_b$. A1, B2 and $D8_b$ phases were also observed following exposure at 700°C, in addition to fine-scale A2 precipitates, which appeared throughout the B2 DR. The majority of the phases observed in this alloy are thought to be representative of the equilibrium microstructures. However, the fine-scale nature of the Cr-rich precipitates, which formed in the DR of the 1200 and 700°C exposed specimens, indicated that they may have formed on cooling. Therefore, to better understand the phase stability of this alloy, DSC was conducted on the homogenised material to establish the phase transition temperatures. The resulting DSC data, displayed in Fig. 11, revealed two large endothermic events on heating. The first began at 595°C and was immediately followed by an exothermic peak, and the second began at 940°C. These thermal events were in good agreement with those observed by Strumza & Hayun [66] and Wang et al. [9] in as-cast $Al_{1.0}$ material. Following detailed investigations, Strumza & Hayun concluded that the lower temperature event corresponded to the formation of the $D8_b$ & A1 phases and the dissolution of the A2 phase, and the higher temperature event was due to the formation of the A2 phase and the dissolution of the $D8_b$ phase. To confirm this, DSC data was also obtained from the 850°C material, which already contained A1 and $D8_b$. This was plotted alongside the DSC data for the homogenised material in Fig. 11. As expected, only the higher temperature endothermic event, corresponding to the $D8_b$ solvus, was observed in the 850°C DSC data. The 850°C DSC data also contained a small exothermic event, which extended from ~790 – 900°C. This may be due to the re-formation of a small amount of A1 or $D8_b$ phase that dissolved during heating below 595°C. It should also be noted that both sets of DSC data featured a small exothermic event at around 1150°C, which has previously been attributed to the A2 solvus [66]. However, all the phases which were present at 1000°C were also observed at 1200°C, so it is not clear what is driving this thermal event.
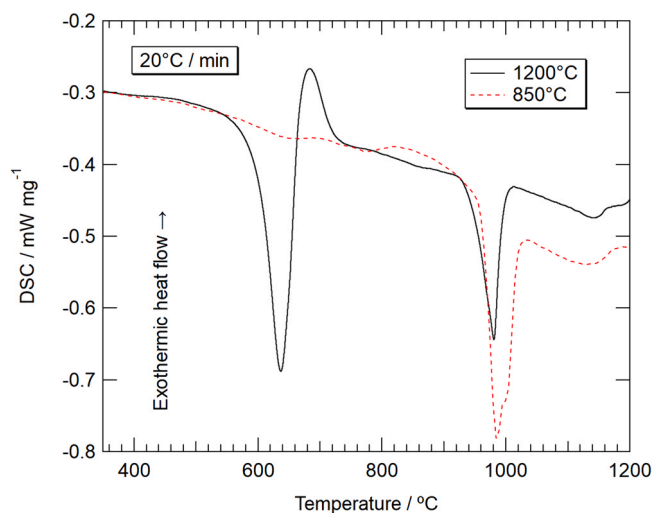

Fig. 11. DSC thermograms from samples of AlCrFeCoNi in the homogenised (1200°C / 72 h) and 850°C / 1000 h conditions obtained whilst heating to 1200°C at a rate of 20°C / min.

The phase transformation temperatures determined by DSC showed good agreement with the phases observed at 850 and 1000°C. At 850°C, the AlCrFeCoNi alloy contained B2, $D8_b$ and A1 phases, whereas at 1000°C, just above the $D8_b$ solvus, there was no evidence of the $D8_b$ phase. The transformation temperatures also showed good agreement with Munitz et al. [45], who observed B2, $D8_b$ and A1 phases following a 3 h heat-treatment at 850°C and also reported some residual $D8_b$ phase at 950°C. However, following 3 h exposures at 975 and 1100°C, the $D8_b$ phase was completely substituted by an A2 phase. The results are also in agreement with Lim et al. [22] who observed A1 and $D8_b$ precipitates at 600 and 700°C, and Panda et al. [47], who also found evidence of both $D8_b$ and A1 precipitates at 800 and 900°C, and only A1 precipitates at 1000 and 1100°C. Favourable comparisons can also be made with a systematic study of Al_x alloys, carried out by Wang et al. [9], in which XRD reflections consistent with an A1 phase were observed at temperatures ≥ 600°C and $D8_b$ reflections were observed between 600 and 900°C. It should also be noted that Munitz et al. [45] and Panda et al. [47] also reported the A2 phase in the temperature range 800 – 900°C [45,47]. However, in both cases phase identification was based solely on laboratory XRD data, which cannot necessarily distinguish the A2 from the B2 phase.

The DSC results also helped to establish the stability of the fine-scale phases observed in the homogenised and 700°C conditions. Firstly, the $D8_b$ phase was identified following homogenisation at 1200°C and after subsequent heat-treatments at 850 and 700°C. However, as reported elsewhere [9,11,36,47,65], no evidence of this phase was found following heat-treatment at 1000°C. Moreover, the DSC data showed that the $D8_b$ solvus was approximately 940°C. Therefore, it is clear that the phase could not have been stable at 1200°C and must have formed during cooling. Secondly, in the 700°C condition, nm-scale coherent Cr-rich precipitates, characteristic of the A2 phase, were present throughout the B2 DR. Similar precipitates have also been observed following heat-treatment of as-cast material at 700°C for 6 [22] and 1000 h [36]. In both cases the precipitates were conclusively identified as A2. However, the DSC data presented in Fig. 11 and in Fig. 18a of reference [66], indicated that the A2 phase is not stable at this temperature, so also must have formed during cooling. Fine-scale DR precipitates, characteristic of the A2 phase, were also present in the homogenised condition. However, in this case, the ID were also majority A2, indicating that the phase was thermodynamically stable at the exposure temperature. Therefore, the precipitation of the A2 in the DR is believed to
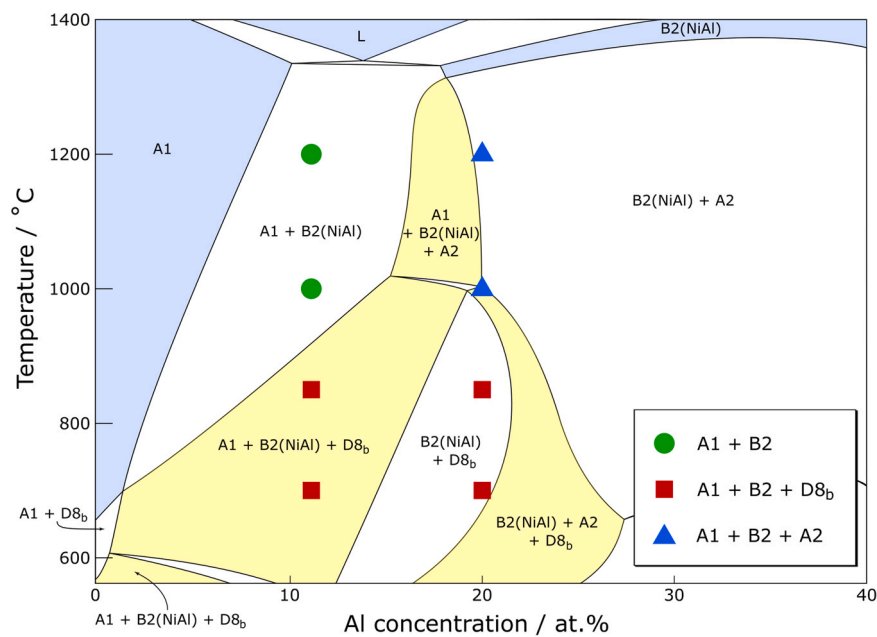
Fig. 12. Thermodynamically predicted isopleth showing the influence of Al content on the phase equilibria of Al$_x$CrFeCoNi alloys.

have been driven by a supersaturation of the B2 DR matrix on cooling. This could also account for the fact that Cr-rich precipitates formed in the DR on cooling from 1200 and 700 but not from 1000 or 850°C (Fig. 7), since the latter alloys contained large Cr-rich DR precipitates, which are likely to have depleted the DR regions of Cr. Indeed, EDX measurements showed that the B2 DR in the 1200 and 700°C alloys contained 16% Cr, versus 8% and 5% in the 1000°C and 850°C specimens, respectively. Therefore, the formation of the Cr-rich A2 and D8$_b$ phases on quenching appears to have been driven by a supersaturation of the Cr within the B2 DR phase.

4.2. Accuracy of thermodynamic predictions

Thermodynamic calculations, performed using the TCHEA4 CALPHAD database, were used to generate a predicted pseudo-binary phase diagram for the Al$_x$CrFeCoNi system, displayed in Fig. 12. According to the predictions, at low Al concentrations, the alloy solidifies into a single A1 phase field, which persists to below 700°C in the Al-free quaternary. However, as the Al concentration is increased, the solvus temperatures of the AlNi-B2 and D8$_b$ phases increase and the solidus temperature decreases. The B2 solvus, which rises more steeply than the D8$_b$ solvus, eventually meets the solidus creating a eutectic isotherm at ~1333°C, between 10 and 18 at.% Al, with a eutectic composition of 13.8 at.%. As a result, the Al$_{0.5}$ alloy is predicted to solidify with an A1 + B2 hypoeutectic microstructure, which persists until the D8$_b$ solvus at 916°C. With a further increase in Al concentration, the A2 phase becomes stable at high temperatures, creating a three phase A1 + B2 + A2 region. However, below ~1000°C the A2 phase is substituted for D8$_b$ and as the temperature decreases further, the A1 phase is also no longer stable, leaving just the B2 and D8$_b$ phases. The Al$_{1.0}$ alloy solidifies into a narrow B2 phase field, beneath which lies a B2 + A2 phase field. As the temperature decreases further, the alloy passes very close to the predicted A1 solvus before crossing the D8$_b$ solvus at ~1000°C. At a slightly lower temperature, the alloy enters a B2 + D8$_b$ phase field that extends to below 700°C. Further increases in the Al concentration result in a strong suppression of the D8$_b$ solvus and a gradual increase in the solidus temperature. In the following section, these thermodynamic predictions are compared with the literature data compiled in Fig. 1 and the experimental results presented in

this study, with two objectives: Firstly, to build a more complete picture of phase stability within the Al$_x$ system; and secondly, to assess the veracity of the thermodynamic database.

4.3. Comparison with literature data

In general, the literature data displayed in Fig. 1, showed good agreement with the predictions of TCHEA4. Several studies have verified the existence of a single A1 phase above 656°C in the CrFeCoNi alloy [2,12,32,34,72], and in alloys containing low Al concentrations [2,73,74]. The experimental observations also agreed well with the predicted B2 solvus, though comparative data was sparse below 1000°C. Furthermore, save a single exception where D8$_b$ formed during slow cooling [43], all experimental observations of the D8$_b$ phase lie beneath the predicted D8$_b$ solvus. However, there was some disagreement about the stability of the A2 phase, with several studies reporting the A2 phase outside of the temperature and compositional ranges predicted. This included Al$_{0.7}$ at 1250°C [30], Al$_{0.5}$ at 850°C [53], and Al$_{1.0}$ following exposure at temperatures between 974 and 670°C, where only B2 and D8$_b$ phases are predicted [22,36,45,47]. However, closer examination of these studies showed that some might not provide an accurate picture of the phase stability. In the first instance, following 1000 h at 1250°C, Zhang *et al.* [30] used atom probe tomography to reveal the presence of nm-scale A2 precipitates within the B2 phase of a Al$_{0.7}$ dual-phase A1 + B2 alloy. The precipitates contained ~86 at.% Cr and ~7 at.% Fe & Co, respectively, which clearly distinguished them from the B2 and A1 phases. However, the fine-scale nature of the precipitates suggests that they could have formed on cooling; especially considering that no quench procedure was specified, and the thermodynamic predictions indicate that the A2 is only stable below ~550°C. In the second instance, Wang *et al.* [53] identified the phases in the Al$_{0.5}$ alloy, following exposure at 850°C for 8 h. The heat-treated specimen contained XRD reflections consistent with an A1 and a B2 phase. In addition, SADPs were acquired from two precipitates, which were indexed as B2 and A2, respectively. However, the SADP which was indexed as A2 was acquired in the [$\bar{1}$11] direction. In this orientation, superlattice reflections do not appear, so it is impossible to distinguish between A2 and B2 structures with the same lattice parameters. As such, there was insufficient evidence

to conclude that the specimen contained the A2 phase. The third instance concerns reports of an A2 phase between 974 and 670°C in the $Al_{1.0}$ alloy [22,36,45,47], which were previously reviewed in Section 4.1. Evidence of an A2 phase was only found at 700°C [22,36], where, as in the present study, it is thought to have formed on cooling. As such, there is no convincing evidence in the literature data to question the veracity of the thermodynamic predictions for the A2 phase. In contrast, literature data indicated that the stability of the A1 phase was underestimated as the Al concentration approached the equiatomic composition. The predictions indicated that the A1 phase was not stable in alloys with an Al atomic ratio ≥ 1.0. However, literature studies have consistently reported the A1 phase in the $Al_{1.0}$ alloy [2,11,22,45,47,65]. Above 1000°C, the $Al_{1.0}$ alloy composition is close to the A1 + B2 + A2 phase field, so the disagreement is slight, but at lower temperatures the predicted A1 solvus shifted to lower Al concentrations and there was a significant divergence between the literature and the thermodynamic predictions [9,22,45,47]. The $L1_2$ phase also appeared to be more stable than predicted by TCHEA4. This phase has been observed following exposure at temperatures up to 700°C in the $Al_{0.3}$ alloy [15,19–21,35,59,75] but was only predicted below ~ 550°C. In general, there was little agreement between the phases reported in the literature and thermodynamic predictions below 600°C. However, experimental investigations in this low temperature regime should be treated with caution as the slow kinetics can delay the formation of detectable quantities of precipitate phases for many hundreds of hours [12,30,31]. Although, experimental investigations employing heat-treatments of up to 1000 h have uncovered no convincing evidence of the additional phases that are predicted below 656°C in the CrFeCoNi alloy [32,33,76,77].

4.4. Comparison with present results

A comparison of the present results with the thermodynamic predictions allowed a more rigorous assessment of the veracity of the TCHEA4 database. For ease of comparison, markers denoting the experimentally observed phases were overlaid onto the predicted pseudo-binary phase diagram in Fig. 12. Green circles represented A1 + B2, red squares for A1 + B2 + $D8_b$, and blue triangles for A1 + B2 + A2. Overall, the predictions reflected the experimental observations reasonably well. For the $Al_{0.5}$ alloy, the database perfectly predicted the experimentally observed phases across all the temperatures investigated. For the $Al_{1.0}$ alloy, TCHEA4 also correctly predicted that the A2 phase was substituted by the $D8_b$ phase below 1000°C, and the predicted solvus temperature for the $D8_b$ phase, 974°C, was close to the solvus temperature measured by DSC (940°C). However, the thermodynamic predictions for the $Al_{1.0}$ alloy did not accurately reflect all the phases observed in any of the conditions investigated. Experimental investigations showed that the homogenised (1200°C) and 1000°C heat-treated specimens were comprised of B2, A2 and A1 phases but the database predicted a dual phase B2 + A2 microstructure at 1200°C and B2, A2 and $D8_b$ phases at 1000°C. However, it is worth pointing out that both these conditions were close to the predicted B2 + A2 + A1 phase field, so an extension of the A1 + B2 + A2 phase field to correct for these discrepancies should only require a small adjustment of the thermodynamic parameters describing the $D8_b$ and A1 phases. At the lower temperatures of 850 and 700°C, the thermodynamic database correctly predicted the formation of the B2 and $D8_b$ phases, but as was found with the literature data, it significantly under-predicted the stability of the A1 phase. The database also predicted a B2 + A2 + $D8_b$ phase field below 670°C, followed by a B2 + A2 below 545°C, though our DSC analysis indicated that the dissolution of the A2 phase and formation of A1 and $D8_b$ phases occurred in the temperature range 595 – 665°C on heating.

5. Conclusions

This study has sought to develop our understanding of phase stability within the Al_xCrFeCoNi alloy system. Firstly, the current knowledge of phase stability in this system was systematically reviewed. Additional experimental investigations, involving long-duration heat-treatments at intermediate temperatures, were then undertaken to better establish the equilibrium phase stability of the $Al_{0.5}$ and $Al_{1.0}$ alloys. Alongside existing literature, these experimental observations were used to assess the veracity of CALPHAD predictions of a current thermodynamic database.

The addition of Al to the CrFeCoNi alloy promoted the formation of the B2 and $D8_b$ phases. Observations of both these phases in the literature and the present study showed good agreement with the thermodynamic predictions of TCHEA4. Specifically, in the $Al_{0.5}$ alloy, a dual phase A1 + B2 microstructure was observed at 1000°C and above but $D8_b$ phase precipitates were identified following heat-treatment at lower temperatures. An $L1_2$ phase has also reported at temperatures up to 700°C in alloys containing ~ 3–15 at.% Al. While this phase was predicted at lower temperatures, its stability appears to have been underestimated. As the Al contents approached the equiatomic ratio, an A2 phase also became stable at higher and lower temperatures, whilst the $D8_b$ phase remained dominant in the intermediate temperature range. In the $Al_{1.0}$ alloy, A1, B2 and A2 phases formed above 940°C but at lower temperatures the A2 phase was substituted by $D8_b$, showing reasonable agreement with the predicted $D8_b$ solvus. Furthermore, below 595°C, the $D8_b$ and A1 phases are replaced by the A2 phase. Therefore, contrary to the thermodynamic predictions, the A1 phase formed between 595 and 1200°C in the $Al_{1.0}$ alloy. This discrepancy was particularly significant at lower temperatures. In summary, where appropriate experimental phase stability information was available for comparison, the TCHEA4 database performed reasonably well. However, further experimental investigations are needed to test the predictions in areas where little or no comparative data presently exists.

Data Availability

The underlying research data associated with this work is available from the University of Cambridge repository (doi: 10.17863/ CAM.87159).

Declaration of Competing Interest

The authors declare that they have no known competing financial interests or personal relationships that could have appeared to influence the work reported in this paper.

References

[1] Z. Tang, M.C. Gao, H. Diao, T. Yang, J. Liu, T. Zuo, Y. Zhang, Z. Lu, Y. Cheng, Y. Zhang, K.A. Dahmen, P.K. Liaw, T. Egami, Aluminum alloying effects on lattice types, microstructures, and mechanical behavior of high-entropy alloys systems, JOM 65 (2013) 1848–1858, https://doi.org/10.1007/s11837-013-0776-z

[2] Y.F. Kao, T.J. Chen, S.K. Chen, J.W. Yeh, Microstructure and mechanical property of as-cast, -homogenized, and -deformed Al$_x$CoCrFeNi (0 ≤ x ≤ 2) high-entropy alloys, J. Alloy. Compd. 488 (2009) 57–64, https://doi.org/10.1016/j.jallcom.2009.08.090

[3] C. Li, J.C. Li, M. Zhao, Q. Jiang, Effect of aluminum contents on microstructure and properties of Al$_x$CoCrFeNi alloys, J. Alloy. Compd. 504 (2010) S515–S518, https://doi.org/10.1016/j.jallcom.2010.03.111

[4] D. Li, C. Li, T. Feng, Y. Zhang, G. Sha, J.J. Lewandowski, P.K. Liaw, Y. Zhang, High-entropy Al$_{0.3}$CoCrFeNi alloy fibers with high tensile strength and ductility at ambient and cryogenic temperatures, Acta Mater. 123 (2017) 285–294, https://doi.org/10.1016/j.actamat.2016.10.038

[5] S.Q. Xia, X. Yang, T.F. Yang, S. Liu, Y. Zhang, Irradiation resistance in Al$_x$CoCrFeNi high entropy alloys, JOM 67 (2015) 2340–2344, https://doi.org/10.1007/s11837-015-1568-4

[6] S. Praveen, H.S. Kim, High-entropy alloys: potential candidates for high-temperature applications - an overview, Adv. Eng. Mater. 20 (2018) 1700645, https://doi.org/10.1002/adem.201700645

[7] Q. Wu, Z. Wang, X. Hu, T. Zheng, Z. Yang, F. He, J. Li, J. Wang, Uncovering the eutectics design by machine learning in the Al–Co–Cr–Fe–Ni high entropy system, Acta Mater. 182 (2020) 278–286, https://doi.org/10.1016/j.actamat.2019.10.043

[8] W.R. Wang, W.L. Wang, S.C. Wang, Y.C. Tsai, C.H. Lai, J.W. Yeh, Effects of Al addition on the microstructure and mechanical property of Al$_x$CoCrFeNi high-entropy alloys, Intermetallics 26 (2012) 44–51, https://doi.org/10.1016/j.intermet.2012.03.005

[9] W-R. Wang, W-L. Wang, J-W. Yeh, Phases, microstructure and mechanical properties of Al$_x$CoCrFeNi high-entropy alloys at elevated temperatures, J. Alloy. Compd. 589 (2014) 143–152, https://doi.org/10.1016/j.jallcom.2013.11.084

[10] H.-P. Chou, Y.-S. Chang, S.-K. Chen, J-W. Yeh, Microstructure, thermophysical and electrical properties in Al$_x$CoCrFeNi (0≤x≤2) high-entropy alloys, Mater. Sci. Eng. B 163 (2009) 184–189, https://doi.org/10.1016/j.mseb.2009.05.024

[11] K. Jasiewicz, J. Cieslak, S. Kaprzyk, J. Tobola, Relative crystal stability of Al$_x$FeNiCrCo high entropy alloys from XRD analysis and formation energy calculation, J. Alloy. Compd. 648 (2015) 307–312, https://doi.org/10.1016/j.jallcom.2015.06.260

[12] J. Cieslak, J. Tobola, K. Berent, M. Marciszko, Phase composition of Al$_x$FeNiCrCo high entropy alloys prepared by sintering and arc-melting methods, J. Alloy. Compd. 740 (2018) 264–272, https://doi.org/10.1016/j.jallcom.2017.12.333

[13] M. Annasamy, N. Haghdadi, A. Taylor, P. Hodgson, D. Fabijanic, Dynamic recrystallization behaviour of Al$_x$CoCrFeNi high entropy alloys during high-temperature plane strain compression, Mater. Sci. Eng. A 745 (2019) 90–106, https://doi.org/10.1016/j.msea.2018.12.102

[14] M. Li, J. Gazquez, A. Borisevich, R. Mishra, K.M. Flores, Evaluation of microstructure and mechanical property variations in Al$_x$CoCrFeNi high entropy alloys produced by a high-throughput laser deposition method, Intermetallics 95 (2018) 110–118, https://doi.org/10.1016/j.intermet.2018.01.021

[15] T.-T. Shun, Y.-C. Du, Microstructure and tensile behaviors of FCC Al$_{0.3}$CoCrFeNi high entropy alloy, J. Alloy. Compd. 479 (2009) 157–160, https://doi.org/10.1016/j.jallcom.2008.12.088

[16] C.M. Lin, H.L. Tsai, Evolution of microstructure, hardness, and corrosion properties of high-entropy Al$_{0.5}$CoCrFeNi alloy, Intermetallics 19 (2011) 288–294, https://doi.org/10.1016/j.intermet.2010.10.008

[17] M. Annasamy, N. Haghdadi, A. Taylor, P. Hodgson, D. Fabijanic, Static recrystallization and grain growth behaviour of Al$_{0.3}$CoCrFeNi high entropy alloy, Mater. Sci. Eng. A 754 (2019) 282–294, https://doi.org/10.1016/j.msea.2019.03.088

[18] H.Y. Yasuda, H. Miyamoto, K. Cho, T. Nagase, Formation of ultrafine-grained microstructure in Al$_{0.3}$CoCrFeNi high entropy alloys with grain boundary precipitates, Mater. Lett. 199 (2017) 120–123, https://doi.org/10.1016/j.matlet.2017.04.072

[19] B. Gwalani, S. Gorsse, D. Choudhuri, Y. Zheng, R.S. Mishra, R. Banerjee, Tensile yield strength of a single bulk Al$_{0.3}$CoCrFeNi high entropy alloy can be tuned from 160 MPa to 1800 MPa, Scr. Mater. 162 (2019) 18–23, https://doi.org/10.1016/j.scriptamat.2018.10.023

[20] B. Gwalani, S. Gorsse, D. Choudhuri, M. Styles, Y. Zheng, R.S. Mishra, R. Banerjee, Modifying transformation pathways in high entropy alloys or complex concentrated alloys via thermo-mechanical processing, Acta Mater. 153 (2018) 169–185, https://doi.org/10.1016/j.actamat.2018.05.009

[21] B. Gwalani, V. Soni, M. Lee, S.A. Mantri, Y. Ren, R. Banerjee, Optimizing the coupled effects of Hall-Petch and precipitation strengthening in a Al$_{0.3}$CoCrFeNi high entropy alloy, Mater. Des. 121 (2017) 254–260, https://doi.org/10.1016/j.matdes.2017.02.072

[22] K.R. Lim, K.S. Lee, J.S. Lee, J.Y. Kim, H.J. Chang, Y.S. Na, Dual-phase high-entropy alloys for high-temperature structural applications, J. Alloy. Compd. 728 (2017) 1235–1238, https://doi.org/10.1016/j.jallcom.2017.09.089

[23] Z. Li, S. Zhao, H. Diao, P.K. Liaw, M.A. Meyers, High-velocity deformation of Al$_{0.3}$CoCrFeNi high-entropy alloy: Remarkable resistance to shear failure, Sci. Rep. 7 (2017) 1–8, https://doi.org/10.1038/srep42742

[24] A. Manzoni, H. Daoud, R. Völkl, U. Glatzel, N. Wanderka, Phase separation in equiatomic AlCoCrFeNi high-entropy alloy, Ultramicroscopy 132 (2013) 212–215, https://doi.org/10.1016/j.ultramic.2012.12.015

[25] Y. Lv, R. Hu, Z. Yao, J. Chen, D. Xu, Y. Liu, X. Fan, Cooling rate effect on microstructure and mechanical properties of Al$_x$CoCrFeNi high entropy alloys, Mater. Des. 132 (2017) 392–399, https://doi.org/10.1016/j.matdes.2017.07.008

[26] Y. Ma, Q. Wang, B.B. Jiang, C.L. Li, J.M. Hao, X.N. Li, C. Dong, T.G. Nieh, Controlled formation of coherent cuboidal nanoprecipitates in body-centered cubic high-entropy alloys based on Al$_2$(Ni,Co,Fe,Cr)$_{14}$ compositions, Acta Mater. 147 (2018) 213–225, https://doi.org/10.1016/j.actamat.2018.01.050

[27] C. Li, M. Zhao, J.C. Li, Q. Jiang, B2 structure of high-entropy alloys with addition of Al, J. Appl. Phys. 104 (2008) 113504, https://doi.org/10.1063/1.3032900

[28] Y.J. Zhou, Y. Zhang, Y.L. Wang, G.L. Chen, Solid solution alloys of AlCoCrFeNiTi$_x$ with excellent room-temperature mechanical properties, Appl. Phys. Lett. 90 (2007) 181904, https://doi.org/10.1063/1.2734517

[29] T. Yang, S. Xia, S. Liu, C. Wang, S. Liu, Y. Zhang, J. Xue, S. Yan, Y. Wang, Effects of Al addition on microstructure and mechanical properties of Al$_x$CoCrFeNi High-entropy alloy, Mater. Sci. Eng. A 648 (2015) 15–22, https://doi.org/10.1016/j.msea.2015.09.034

[30] C. Zhang, F. Zhang, H. Diao, M.C. Gao, Z. Tang, J.D. Poplawsky, P.K. Liaw, Understanding phase stability of Al-Co-Cr-Fe-Ni high entropy alloys, Mater. Des. 109 (2016) 425–433, https://doi.org/10.1016/j.matdes.2016.07.073

[31] K. Srimark, S. Dasari, A. Sharma, P. Wangyao, B. Gwalani, T. Rojhirunsakool, S. Gorsse, R. Banerjee, Hierarchical phase evolution in a lamellar Al$_{0.7}$CoCrFeNi high entropy alloy involving competing metastable and stable phases, Scr. Mater. 204 (2021) 114137, https://doi.org/10.1016/j.scriptamat.2021.114137

[32] K.A. Christofidou, E.J. Pickering, P. Orsatti, P.M. Mignanelli, T.J.A. Slater, H.J. Stone, N.G. Jones, On the influence of Mn on the phase stability of the CrMn$_x$FeCoNi high entropy alloys, Intermetallics 92 (2018) 84–92, https://doi.org/10.1016/j.intermet.2017.09.011

[33] M.S. Lucas, G.B. Wilks, L. Mauger, J.A. Muñoz, O.N. Senkov, E. Michel, J. Horwath, S.L. Semiatin, M.B. Stone, D.L. Abernathy, E. Karapetrova, Absence of long-range chemical ordering in equimolar FeCoCrNi, Appl. Phys. Lett. 100 (2012) 251907, https://doi.org/10.1063/1.4730327

[34] M. Vaidya, K. Guruvidyathri, B.S. Murty, Phase formation and thermal stability of CoCrFeNi and CoCrFeMnNi equiatomic high entropy alloys, J. Alloy. Compd. 774 (2019) 856–864, https://doi.org/10.1016/j.JALLCOM.2018.09.342

[35] S. Gangireddy, B. Gwalani, V. Soni, R. Banerjee, R.S. Mishra, Contrasting mechanical behavior in precipitation hardenable Al$_x$CoCrFeNi high entropy alloy microstructures: Single phase FCC vs. dual phase FCC-BCC, Mater. Sci. Eng. A 739 (2019) 158–166, https://doi.org/10.1016/j.msea.2018.10.021

[36] T.M. Butler, M.L. Weaver, Investigation of the phase stabilities in AlNiCoCrFe high entropy alloys, J. Alloy. Compd. 691 (2017) 119–129, https://doi.org/10.1016/J.JALLCOM.2016.08.121

[37] B. Kombaiah, K. Jin, H. Bei, P.D. Edmondson, Y. Zhang, Phase stability of single phase Al$_{0.12}$CrNiFeCo high entropy alloy upon irradiation, Mater. Des. 160 (2018) 1208–1216, https://doi.org/10.1016/j.matdes.2018.11.006

[38] Y.C. Huang, C.S. Tsao, C. Lin, Y.C. Lai, S.K. Wu, C.H. Chen, Evolution of Guinier-Preston zones in cold-rolled Al$_{0.2}$CoCrFeNi high-entropy alloy studied by synchrotron small-angle X-ray scattering, Mater. Sci. Eng. A 769 (2020) 138526, https://doi.org/10.1016/j.msea.2019.138526

[39] B. Gwalani, V. Soni, D. Choudhuri, M. Lee, J.Y. Hwang, S.J. Nam, H. Ryu, S.H. Hong, R. Banerjee, Stability of ordered L1$_2$ and B2 precipitates in face centered cubic based high entropy alloys - Al$_{0.3}$CoFeCrNi and Al$_{0.3}$CuFeCrNi$_2$, Scr. Mater. 123 (2016) 130–134, https://doi.org/10.1016/J.SCRIPTAMAT.2016.06.019

[40] D. Choudhuri, B. Gwalani, S. Gorsse, M. Komarasamy, S.A. Mantri, S.G. Srinivasan, R.S. Mishra, R. Banerjee, Enhancing strength and strain hardenability via deformation twinning in fcc-based high entropy alloys reinforced with intermetallic compounds, Acta Mater. 165 (2019) 420–430, https://doi.org/10.1016/j.actamat.2018.12.010

[41] K. Liu, M. Komarasamy, B. Gwalani, S. Shukla, R.S. Mishra, Fatigue behavior of ultrafine grained triplex Al$_{0.3}$CoCrFeNi high entropy alloy, Scr. Mater. 158 (2019) 116–120, https://doi.org/10.1016/j.scriptamat.2018.08.048

[42] M. Chen, L. Lan, X. Shi, H. Yang, M. Zhang, J. Qiao, The tribological properties of Al$_{0.6}$CoCrFeNi high-entropy alloy with the σ phase precipitation at elevated temperature, J. Alloy. Compd. 777 (2019) 180–189, https://doi.org/10.1016/j.jallcom.2018.10.393

[43] Z. Tang, O.N. Senkov, C.M. Parish, C. Zhang, F. Zhang, L.J. Santodonato, G. Wang, G. Zhao, F. Yang, P.K. Liaw, Tensile ductility of an AlCoCrFeNi multi-phase high-entropy alloy through hot isostatic pressing (HIP) and homogenization, Mater. Sci. Eng. A 647 (2015) 229–240, https://doi.org/10.1016/j.msea.2015.08.078

[44] H.R. Sistla, J.W. Newkirk, F. Frank Liou, Effect of Al/Ni ratio, heat treatment on phase transformations and microstructure of Al$_x$FeCoCrNi$_{2-x}$ (x=0.3, 1) high entropy alloys, Mater. Des. 81 (2015) 113–121, https://doi.org/10.1016/j.matdes.2015.05.027

[45] A. Munitz, S. Salhov, S. Hayun, N. Frage, Heat treatment impacts the microstructure and mechanical properties of AlCoCrFeNi high entropy alloy, J. Alloy. Compd. 683 (2016) 221–230, https://doi.org/10.1016/j.jallcom.2016.05.034

[46] C.D. Gómez-Esparza, J. Camarillo-Cisneros, I. Estrada-Guel, J.G. Cabañas-Moreno, J.M. Herrera-Ramírez, R. Martínez-Sánchez, Effect of Cr, Mo and Ti on the microstructure and Vickers hardness of multi-component systems, J. Alloy. Compd. 615 (2015) S638–S644, https://doi.org/10.1016/j.jallcom.2014.01.081

[47] J.P. Panda, P. Arya, K. Guruvidyathri, B.S.Murty Ravikirana, Studies on kinetics of BCC to FCC phase transformation in AlCoCrFeNi equiatomic high entropy alloy, Metall. Mater. Trans. A (2021) 1–10, https://doi.org/10.1007/s11661-021-06162-3

[48] J.C. Rao, H.Y. Diao, V. Ocelík, D. Vainchtein, C. Zhang, C. Kuo, Z. Tang, W. Guo, J.D. Poplawsky, Y. Zhou, P.K. Liaw, J.T.M.De Hosson, Secondary phases in Al_xCoCrFeNi high-entropy alloys: an in-situ TEM heating study and thermodynamic appraisal, Acta Mater. 131 (2017) 206–220, https://doi.org/10.1016/j.actamat.2017.03.066

[49] C.R. Reynolds, Z. Herl, N.A. Ley, D. Choudhuri, J.T. Lloyd, M.L. Young, Comparing CALPHAD predictions with high energy synchrotron radiation X-ray diffraction measurements during in situ annealing of $Al_{0.3}$CoCrFeNi high entropy alloy, Materialia 12 (2020) 100784, https://doi.org/10.1016/j.mtla.2020.100784

[50] O. Stryzhyboroda, V.T. Witusiewicz, S. Gein, D. Röhrens, U. Hecht, Phase equilibria in the Al–Co–Cr–Fe–Ni high entropy alloy system: thermodynamic description and experimental study, Front. Mater. 7 (2020) 270, https://doi.org/10.3389/FMATS.2020.00270/BIBTEX

[51] S.-Z. Niu, H.-C. Kou, J. Wang, J.-S. Li, Improved tensile properties of $Al_{0.5}$CoCrFeNi high-entropy alloy by tailoring microstructures, Rare Met 1–6 (2017), https://doi.org/10.1007/s12598-016-0860-y

[52] Y. Zhang, J. Li, J. Wang, S. Niu, H. Kou, Hot deformation behavior of As-cast and homogenized $Al_{0.5}$CoCrFeNi high entropy alloys, Metals 6 (2016) 277, https://doi.org/10.3390/met6110277

[53] J. Wang, S. Niu, T. Guo, H. Kou, J. Li, The FCC to BCC phase transformation kinetics in an $Al_{0.5}$CoCrFeNi high entropy alloy, J. Alloy. Compd. 710 (2017) 144–150, https://doi.org/10.1016/j.jallcom.2017.03.249

[54] J.C. Rao, V. Ocelík, D. Vainchtein, Z. Tang, P.K. Liaw, J.T.M.De Hosson, The fcc-bcc crystallographic orientation relationship in Al_xCoCrFeNi high-entropy alloys, Mater. Lett. 176 (2016) 29–32, https://doi.org/10.1016/j.matlet.2016.04.086

[55] B. Gwalani, T. Wang, A. Jagetia, S. Gangireddy, S. Muskeri, S. Mukherjee, J.T. Lloyd, R. Banerjee, R.S. Mishra, Dynamic shear deformation of a precipitation hardened $Al_{0.7}$CoCrFeNi eutectic high-entropy alloy using hat-shaped specimen geometry, Entropy 22 (2020) 431, https://doi.org/10.3390/e22040431

[56] T.S. Reddy, I.S. Wani, T. Bhattacharjee, S.R. Reddy, R. Saha, P.P. Bhattacharjee, Severe plastic deformation driven nanostructure and phase evolution in a $Al_{0.5}$CoCrFeMnNi dual phase high entropy alloy, Intermetallics 91 (2017) 150–157, https://doi.org/10.1016/j.intermet.2017.09.002

[57] D.M. King, S.C. Middleburgh, L. Edwards, G.R. Lumpkin, M. Cortie, Predicting the crystal structure and phase transitions in high-entropy alloys, JOM 67 (2015) 2375–2380, https://doi.org/10.1007/s11837-015-1495-4

[58] M. Ogura, T. Fukushima, R. Zeller, P.H. Dederichs, Structure of the high-entropy alloy Al CrFeCoNi: fcc versus bcc, J. Alloy. Compd. 715 (2017) 454–459, https://doi.org/10.1016/j.jallcom.2017.04.318

[59] M.S.K.K.Y. Nartu, T. Alam, S. Dasari, S.A. Mantri, S. Gorsse, H. Siller, N. Dahotre, R. Banerjee, Enhanced tensile yield strength in laser additively manufactured $Al_{0.3}$CoCrFeNi high entropy alloy, Materialia 9 (2020) 100522, https://doi.org/10.1016/j.mtla.2019.100522

[60] W. Kai, C.C. Li, F.P. Cheng, K.P. Chu, R.T. Huang, L.W. Tsay, J.J. Kai, Air-oxidation of FeCoNiCr-based quinary high-entropy alloys at 700–900 °C, Corros. Sci. 121 (2017) 116–125, https://doi.org/10.1016/J.CORSCI.2017.02.008

[61] H. Shiratori, T. Fujieda, K. Yamanaka, Y. Koizumi, K. Kuwabara, T. Kato, A. Chiba, Relationship between the microstructure and mechanical properties of an equiatomic AlCoCrFeNi high-entropy alloy fabricated by selective electron beam melting, Mater. Sci. Eng. A 656 (2016) 39–46, https://doi.org/10.1016/j.msea.2016.01.019

[62] C. Li, J.C. Li, M. Zhao, Q. Jiang, Effect of alloying elements on microstructure and properties of multiprincipal elements high-entropy alloys, J. Alloy. Compd. 475 (2009) 752–757, https://doi.org/10.1016/j.jallcom.2008.07.124

[63] A. Vida, L.K. Varga, N.Q. Chinh, D. Molnar, S. Huang, L. Vitos, Effects of the sp element additions on the microstructure and mechanical properties of NiCoFeCr based high entropy alloys, Mater. Sci. Eng. A 669 (2016) 14–19, https://doi.org/10.1016/j.msea.2016.05.082

[64] Y. Sun, C. Wu, H. Peng, Y. Liu, J. Wang, X. Su, Phase constituent and microhardness of As-cast and long-time annealed Al_xCo$_{2−x}$CrFeNi multicomponent alloys, J. Ph. Equilibria Diffus 40 (2019) 706–714, https://doi.org/10.1007/s11669-019-00761-9

[65] E. Ghassemali, R. Sonkusare, K. Biswas, N.P. Gurao, In-situ study of crack initiation and propagation in a dual phase AlCoCrFeNi high entropy alloy, J. Alloy. Compd. 710 (2017) 539–546, https://doi.org/10.1016/j.jallcom.2017.03.307

[66] E. Strumza, S. Hayun, Comprehensive study of phase transitions in equiatomic AlCoCrFeNi high-entropy alloy, J. Alloy. Compd. 856 (2021) 158220, https://doi.org/10.1016/J.JALLCOM.2020.158220

[67] B.D. Cullity, Elements of X-ray diffraction, 3rd ed., Prentice Hall, c2001, New Jersey, USA, 2001.

[68] E.J. Pickering, R. Muñoz-Moreno, H.J. Stone, N.G. Jones, Precipitation in the equiatomic high-entropy alloy CrMnFeCoNi, Scr. Mater. 113 (2016) 106–109, https://doi.org/10.1016/j.scriptamat.2015.10.025

[69] K.A. Christofidou, T.P. McAuliffe, P.M. Mignanelli, H.J. Stone, N.G. Jones, On the prediction and the formation of the sigma phase in CrMnCoFeNi$_x$ high entropy alloys, J. Alloy. Compd. 770 (2018) 285–293, https://doi.org/10.1016/j.jallcom.2018.08.032

[70] M.E. Bloomfield, K.A. Christofidou, N.G. Jones, Effect of Co on the phase stability of CrMnFeCo$_x$Ni high entropy alloys following long-duration exposures at intermediate temperatures, Intermetallics 114 (2019) 106582, https://doi.org/10.1016/J.INTERMET.2019.106582

[71] M.E. Bloomfield, K.A. Christofidou, F. Monni, Q. Yang, M. Hang, N.G. Jones, The influence of Fe variations on the phase stability of CrMnFe$_x$CoNi alloys following long-duration exposures at intermediate temperatures, Intermetallics 131 (2021) 107108, https://doi.org/10.1016/j.intermet.2021.107108

[72] A. Gali, E.P. George, Tensile properties of high- and medium-entropy alloys, Intermetallics 39 (2013) 74–78, https://doi.org/10.1016/j.intermet.2013.03.018

[73] T. Yang, Z. Tang, X. Xie, R. Carroll, G. Wang, Y. Wang, K.A. Dahmen, P.K. Liaw, Y. Zhang, Deformation mechanisms of $Al_{0.1}$CoCrFeNi at elevated temperatures, Mater. Sci. Eng. A 684 (2017) 552–558, https://doi.org/10.1016/j.msea.2016.12.110

[74] D. Li, Y. Zhang, The ultrahigh charpy impact toughness of forged Al_xCoCrFeNi high entropy alloys at room and cryogenic temperatures, Intermetallics 70 (2016) 24–28, https://doi.org/10.1016/j.intermet.2015.11.002

[75] B. Gwalani, V. Soni, D. Choudhuri, M. Lee, J.Y. Hwang, S.J. Nam, H. Ryu, S.H. Hong, R. Banerjee, Stability of ordered L1$_2$ and B2 precipitates in face centered cubic based high entropy alloys - $Al_{0.3}$CoFeCrNi and $Al_{0.3}$CuFeCrNi$_2$, Scr. Mater. 123 (2016) 130–134, https://doi.org/10.1016/j.scriptamat.2016.06.019

[76] F. He, Z. Wang, Q. Wu, J. Li, J. Wang, C.T. Liu, Phase separation of metastable CoCrFeNi high entropy alloy at intermediate temperatures, Scr. Mater. 126 (2017) 15–19, https://doi.org/10.1016/j.scriptamat.2016.08.008

[77] F. He, Z. Wang, B. Han, Q. Wu, D. Chen, J. Li, J. Wang, C.T.T. Liu, J.J.J. Kai, Solid solubility, precipitates, and stacking fault energy of micro-alloyed CoCrFeNi high entropy alloys, J. Alloy. Compd. 769 (2018) 490–502, https://doi.org/10.1016/J.JALLCOM.2018.07.336